ARTICLE

DOI: 10.1590/2317-4889202020190041

BJGEO Brazilian Journal of Geology

Geology, petrology and U-Pb geochronology of metavolcanic rocks in the Mundo Novo greenstone belt, eastern São Francisco Craton, NE Brazil: considerations about its tectonic setting

Ricardo Ramos Spreafico[1,2*], Johildo Salomão Figueiredo Barbosa[1,2], Antônio Marcos Vitória de Moraes[1], Francisco Dias de Souza Júnior[1]

Abstract

Field, petrological and LA-ICP-MS U-Pb geochronological data of metavolcanic rocks were used to interpret the petrological processes and to propose the tectonic setting for the Mundo Novo greenstone belt (MNGB) in the eastern São Francisco Craton. The metavolcanic rocks studied are metakomatiite, eastern and western metabasalts, and metadacite with subordinate metarhyolite, which host ocean floor hydrothermal alteration zones and are covered by ocean floor lithological associations composed of chemical metasedimentary rocks. Fractional crystallization and heterogeneous intraoceanic contaminations explain the mineralogical differences between the two metabasalts and the high $(La/Yb)_N$ ratio values of metakomatiite and metadacite. The metakomatiite and the eastern and western metabasalts feature a vector from the MORB-OIB array to the volcanic arc array in the Nb/Yb-Th/Yb diagram, similar to the Archean intraoceanic arc-basin systems. The geochemical pattern of the eastern and western metabasalts in the Zr-Zr/Y diagram suggests volcanism in nearby island arc and back-arc basin settings, respectively. The 2595 ± 21 Ma U-Pb zircon crystallization age of the metadacite allowed the determination of the timing of volcanism in the MNGB. Therefore, an intraoceanic provenance in an arc-basin system is proposed for the MNGB in the Neoarchean, which was later compressed between cratonic blocks during the Rhyacian-Orosirian event.

KEYWORDS: Mundo Novo greenstone belt; metavolcanic rock; petrology; geochronology; intraoceanic arc-basin system.

INTRODUCTION

The Mundo Novo greenstone belt (MNGB), in the eastern boundary of the Gavião Block (Barbosa and Sabaté 2002, 2003, 2004) and eastern portion of the São Francisco Craton (Figs. 1A and 1B), lies within the Contendas-Jacobina Lineament, NE Brazil (Sabaté *et al.* 1990), which in the area under study is situated between the Gavião and Mairi blocks (Fig. 1C). That greenstone sequence has been a subject of study since the 1970s and hosts the Zn-Pb Fazenda Coqueiro deposit (Mascarenhas *et al.* 1975, Couto *et al.* 1978, Loureiro 1991, Mascarenhas and Silva 1994, Mascarenhas *et al.* 1998, Zincone *et al.* 2016, Reis *et al.* 2017).

Greenstone belts are highly varied Archean geological entities that contain a vast diversity of rocks (Anhaeusser 2014). Generally, their rocks experienced multiple stages of deformation, metamorphism, and metasomatic alteration due to their great age and diversity of geotectonic settings, which were intruded by mafic, ultramafic, and granitoid rocks (Anhaeusser *et al.* 1969, Anhaeusser 2014). Moreover, the intraoceanic or intracontinental provenance of volcanic rocks in Archean greenstone belts has been a recurring discussion topic and whole-rock chemical tools have been constantly applied for such research purposes (Polat and Kerrich 2001, Polat *et al.* 2002, Pearce 2008, 2014).

The predominance of subaqueously deposited basalt and komatiite has been interpreted in a wide variety of geological settings proposed for greenstone belt terrains in intraoceanic crust, ranging from primitive island arcs to plume-related submarine plateaus, mid-ocean ridges (including ophiolites) and back-arc basins (De Wit *et al.* 1987, Storey *et al.* 1988, Parman *et al.* 2001, Chavagnac 2004, Furnes *et al.* 2013). Furthermore, the intraoceanic Archean greenstone belts present a set of evidence as follows: basalt and komatiite occurrence, absence of zircon xenocrysts, mid-ocean ridge basalt (MORB), and island arc tholeiitic (IAT) geochemical patterns, and Th enrichment due to intraoceanic crustal input processes (Pearce 2008). The intraoceanic crustal input, however, would have been

Supplementary material

Supplementary data associated with this article can be found in the online version: Supplementary Data

[1]Companhia Baiana de Pesquisa Mineral – Salvador (BA), Brazil.
E-mails: spreafico.ricardo@gmail.com, johildo.barbosa@gmail.com, amarcosvm@gmail.com, fdsjunior@gmail.com

[2]Universidade Federal da Bahia – Salvador (BA), Brazil.

*Corresponding author.

produced by subduction components, high-grade metamorphism, intraoceanic contamination, crustal recycling, high Th-Nb proxy and delamination (Pearce 2008, 2014).

The metabasalt of the Nova Lima Group in the Archean Rio das Velhas greenstone belt of the southern São Francisco Craton (Fig. 1B), for example, has been considered as derived from an ocean-floor setting based on a pillow lava structure and an association with chemical sediments and volcanic rocks (Zucchetti *et al.* 2000b). Moreover, the geochemical pattern of this metabasalt suggests a submarine plateau setting and

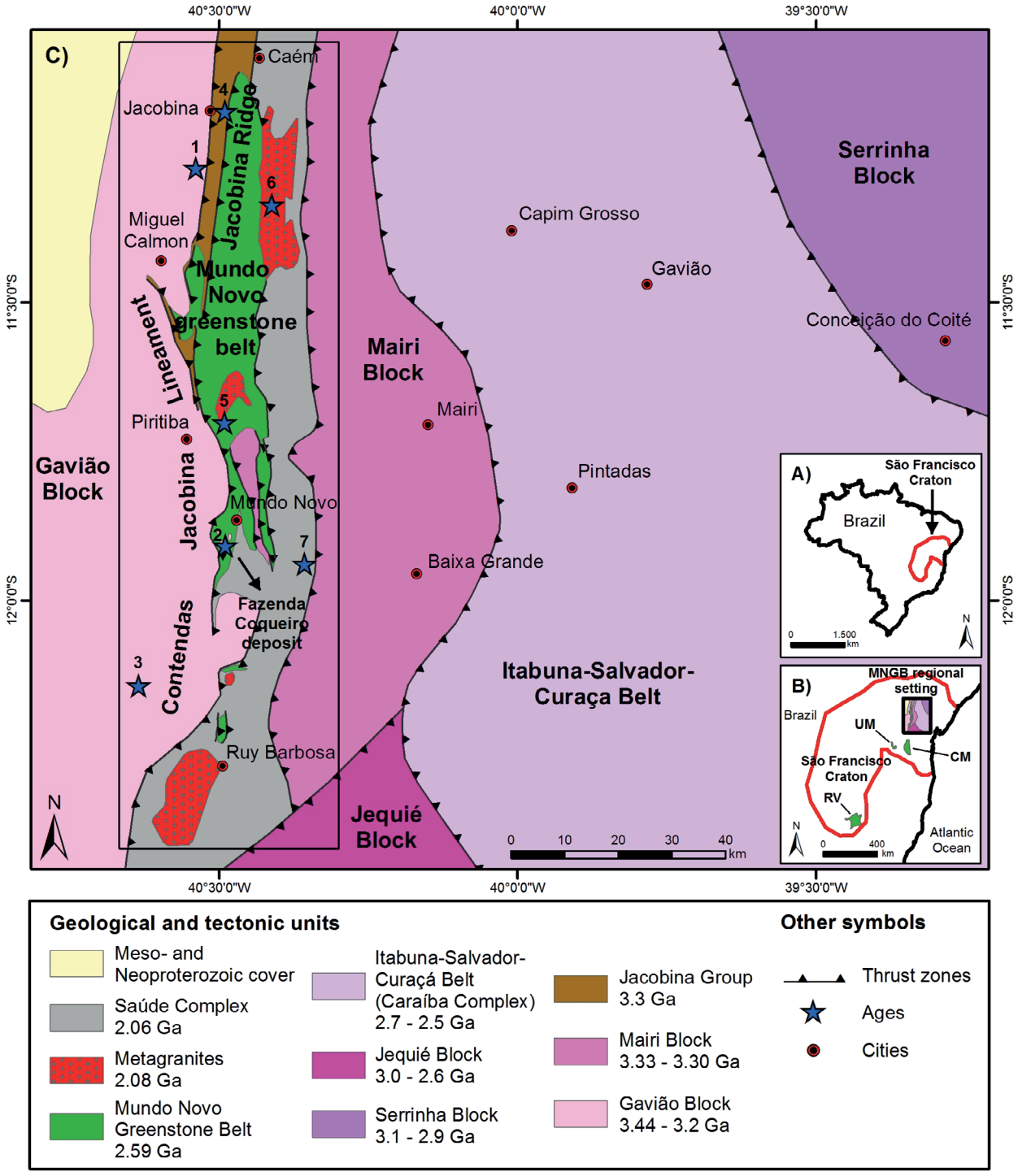

Figure 1. (A) Location of the São Francisco Craton in NE Brazil. (B) Regional geologic context of the MNGB in the eastern portion of the São Francisco Craton and other greenstone belts and volcano-sedimentary sequences: CM: Contendas-Mirante; RV: Rio das Velhas; UM: Umburanas. (C) Regional tectonic setting where the MNGB is inserted (modified from Barbosa and Sabaté 2002, 2003, 2004) and the study area delimited. Ages in the points highlighted on the map: 1- 3442 ± 2 Ma, W. Long.: 40°32'19.11" S. Lat.: 11°16'32.68" (U-Pb zircon, TTG; Mougeot 1996); 2- 3305 ± 9 Ma, W. Long.: 40°29'20.55"/S. Lat.: 11°54'31.06" (U-Pb zircon, metarhyolite from the Gavião Block obtained by Peucat *et al.* 2002) and 3303 ± 11 Ma (U-Pb zircon, metarhyolite from the Gavião Block obtained by Zincone *et al.* 2016); 3- 3292 ± 3 Ma, W. Long.: 40°38'04.57" S. Lat.: 12°08'36.48" (U-Pb zircon, metagranite from the Gavião Block obtained by Zincone *et al.* 2016); 4- 3500–3220 Ma, W. Long.: 40°29'23.61" S. Lat.: 11°10'49.32" (U-Pb zircon, quartzite from the Jacobina Group obtained by Teles *et al.* 2015); 5- 2595 ± 21 Ma, W. Long.: 40°29'26.72" S. Lat.: 11°42'09.52" (U-Pb zircon, metadacite from the MNGB obtained in this work: FD-052 sample); 6- 2080 ± 18 Ma, W. Long.: 40°24'40.64" S. Lat.: 11°20'15.41" (U-Pb monazite, Cachoeira Grande granite obtained by Leite 2002); 7- 2068 ± 12 Ma, W. Long.: 40°21'22.34" S. Lat.: 11°56'21.18" (U-Pb zircon, biotite schist from the Saúde Complex obtained by Zincone *et al.* 2017).

crustal contamination rocks; the felsic volcanic rocks would indicate the presence of an island arc or back-arc type setting (Zucchetti *et al.* 2000a). In the Neoarchean Contendas-Mirante volcano-sedimentary sequence, south of the Contendas-Jacobina Lineament (Fig. 1B), which contains geochemical and age equivalences with the MNGB, intraoceanic basalt occurrences have been interpreted as being related to the banded iron formation (BIF; Rios 2017). The South Abitibi (Kerrich and Xie 2002, Xie and Kerrich 1994), Barberton (Jochum *et al.* 1991, Parman *et al.* 1997, Chavagnac 2004), and Isua (Polat and Hoffmann 2003, Polat *et al.* 2002) are other examples of intraoceanic interpretations for Archean greenstone belts, which Pearce (2008) discusses in his examination of the ocean floor's origin with intraoceanic crustal input along their geological evolution based on a Th-Nb proxy. Despite the contamination issues of analyzing Archean rocks, the geochemical pattern of the modern Mariana Arc, which indicates an arc-basin system in the oceanic crust, was properly used to compare to older intraoceanic settings in the Nb/Yb-Th/Yb diagram (Pearce 2005, 2008).

The intracontinental provenance of volcanic rocks in Archean greenstone belts, on the other hand, has been related to oceanic-continent subduction processes or with the genesis on ensialic settings (Pearce 2008). Greenstones of the Wawa belt in the Superior Province, for example, were formed in an arc-related association (Polat and Kerrich 2001); the Umburanas greenstone belt in the eastern São Francisco Craton (Fig. 1B) was formed over a continental crust (Leal *et al.* 2003). Bickle *et al.* (1994) concluded that the continental provenance for Archean greenstone belts could not easily identify complete ophiolitic sequences, which would thus explain a possible oceanic origin; the presence of zircon xenocrysts, geochemical, and isotopic evidence for crustal contamination, intrusive relationships with older basement rocks and their internal stratigraphy would also indicate continental provenance.

Field, petrographic, whole-rock chemical, and mineral chemistry data were combined with laser ablation inductively coupled plasma mass spectrometry (LA-ICP-MS) U-Pb zircon age from the MNGB. Thus, this study focused on metavolcanic rocks of the lower sequence, which comprise the metakomatiite, and middle sequence of the MNGB, comprising the eastern metabasalt, the metadacite, and the western metabasalt that occur mainly at the Fazenda Coqueiro deposit. The objective was also to propose the age and the tectonic setting of the MNGB regarding the intraoceanic provenance of the volcanic rocks rather than the intracontinental provenance taking into account petrological processes. In addition, the comparison with other Archean greenstone belts and the insertion of the MNGB within the regional geologic context in the eastern portion of the São Francisco Craton, which comprises the Gavião, Mairi, Jequié, and Serrinha blocks and the subsequent tectonic events were also contemplated.

GEOLOGICAL SETTING

The eastern portion of the São Francisco Craton, where the MNGB is situated, was formed through the amalgamation of three Archean blocks during the Paleoproterozoic continent-continent collision (Barbosa and Sabaté 2002, 2003, 2004): the Gavião, Serrinha, and Jequié blocks (Fig. 1C). The Paleoproterozoic event compressed the MNGB and surrounding crust between the cratonic blocks, and the uplift caused by this event possibly resulted in the erosion and the formation of Paleoproterozoic sedimentary basins, such as the uppermost sequence of the MNGB and the Saúde Complex (Zincone *et al.* 2017).

MNGB is in contact to the west with 3.4 Ga (Mougeot 1996) tonalite-trondhjemite-granodiorite (TTG) basement rocks and subordinate metagranites in the Gavião Block and to the east and the south with paragneiss in the Saúde Complex with a maximum age between 2.20 and 2.06 Ga (Zincone *et al.* 2017; Fig. 2). To the north and northwest, the MNGB is in contact with quartzites in the Jacobina Group, which were deposited between 3.55 and 3.22 Ga (Teles *et al.* 2015), and with granitic intrusive aged 2080 ± 18 Ma (Leite 2002).

Additionally, the geological setting includes granulites (3.0 Ga) and multiple charnockite intrusions (2.7 and 2.6 Ga) in the Jequié Block (Wilson 1987, Silva *et al.* 2002), the Itabuna-Salvador-Curaçá Belt (2574 ± 6 and 2695 ± 12 Ma obtained by Oliveira *et al.* 2010, Silva *et al.* 1997; respectively), and the Serrinha Block (3152 ± 5 Ma obtained by Oliveira *et al.* 2002a, 2002b; 2989 ± 11, 3072 ± 2, and 3162 ± 26 Ma obtained by Rios *et al.* 2009); although the Itabuna-Salvador-Curaçá Belt and Serrinha Block are far from the MNGB, they are important to understand the collisional Paleoproterozoic tectonic context of the study area (Figs. 1C and 2). Table 1 shows regional geochronological data from the MNGB and surrounding units.

The eastern margin of the Gavião Block is in tectonic contact with the lithologies of the MNGB (Figs. 1C and 2) and is composed of TTG gneiss and migmatites that host mafic rock enclaves, metagranites, and metarhyolites (Zincone *et al.* 2016). This block corresponds to the basement of the MNGB. Three groups of TTG gneiss are described in the Gavião Block: two groups are trondhjemitic with U-Pb zircon ages (SHRIMP) of 3403 ± 5 and 3158 ± 5 Ma (Barbosa 1997, Leal 1998), and the other group, with granodioritic compositions, includes the 3225 ± 10 Ma Aracatu granitoid (Barbosa *et al.* 2012a). The Gavião Block age, near the MNGB, is 3.4 Ga (Mougeot 1996), but metarhyolites aged 3303 ± 11 Ma (Peucat *et al.* 2002, Zincone *et al.* 2016) and metagranites, such as Boa Sorte at 3291 ± 2.5 Ma, occur as well (Zincone *et al.* 2016).

The Mairi Block, composed of gneiss, migmatites, and granitic and tonalitic orthogneiss, with some occurrences of basic and ultrabasic bodies (Peucat *et al.* 2002) to the east and southeast of the MNGB, is in tectonic contact with thrust zones with a west vergence. The LA-ICP-MS (U-Pb, zircon) ages of 3.33 and 3.30 Ga (Sousa *et al.* 2018) for the orthogneiss in the Mairi Block indicate that this complex is coeval with the Gavião Block and, possibly, the two could have been joined together at the time of their formation.

The Jacobina Group is in tectonic contact with the MNGB along thrust zones, with all zones striking north-south and verging to the west (Figs. 1C and 2) with the Gavião Block in the footwall. The Jacobina Group comprises metaconglomerates that host an important gold deposit, and quartzites, metarenites, phyllites, chlorite schists and quartz-sericite schists

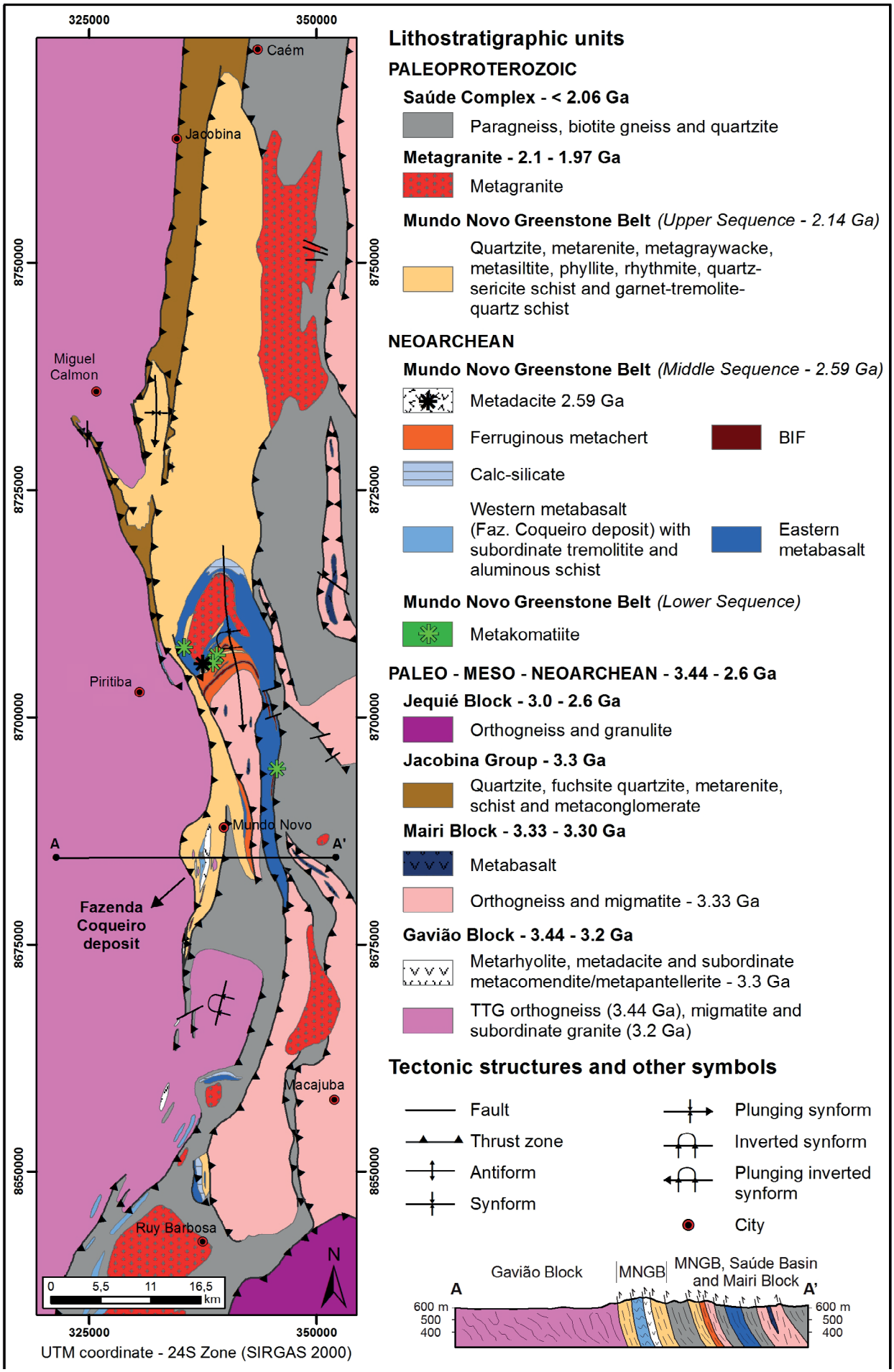

Figure 2. Geological map of the MNGB and adjoining units. Modified and updated from Loureiro (1991), Mascarenhas and Silva (1994), and Souza *et al.* (2002).

(Mascarenhas *et al.* 1998) deposited in a passive margin setting (Reis *et al.* 2018). This group has a depositional age, based on detrital zircons, between 3500 and 3220 Ma (Teles 2013, Teles *et al.* 2015, Barbuena *et al.* 2016), with a large portion of the zircon populations situated between 3.3 and 3.4 Ga (Magee *et al.* 2001, Teles *et al.* 2015). Jacobina Ridge represents an Archean supracrustal sequence, with a maximum age of 3.28 Ga, whose sources are likely rocks from both the plutonic-volcanic system and the TTG suite in the Gavião Block (Zincone *et al.* 2016).

The MNGB, which Zincone *et al.* (2016) referred to as the Mundo Novo supracrustal belt, is inserted into the Contendas-Jacobina Lineament and is divided into three stratigraphic sequences — a lower sequence (ultramafic rocks), a middle sequence (mafic and felsic igneous rocks and clastic and chemical metasedimentary rocks), and an upper one (siliciclastic metasedimentary rocks; Spreafico *et al.* 2018). Carbonate and argilic-chloritic hydrothermal alteration zones in the ocean floor setting have been identified and described in the Fazenda Coqueiro deposit related to Zn-Pb mineralization hosted in the western metabasalt of the middle sequence (Spreafico 2017). Two ductile and compressional and progressive Paleoproterozoic deformational phases in the MNGB, D_1 and D_2, are described in the area in a previous study (Spreafico 2017). The D_1 deformational phase is characterized by isoclinal and recumbent folds vergent to the west that generated greenschist metamorphic facies rocks. The D_2 deformational phase is characterized by a refolding that generated vertical and subvertical axial planes that eventually resulted in the formation of a coaxial interference pattern (Ramsay and Huber 1987) or compressive and transpressive shear zones, which bound the MNGB lithologies and generated greenschist rocks to amphibolite metamorphic facies. The most prominent brittle structures are east-trending faults and fractures. The age of the MNGB has been previously studied, and initial geochronological studies have defined the Neoarchean age of the volcanism (Spreafico *et al.* 2018), such as the sedimentation at the top of the sequence (Barbuena *et al.* 2016), which has a maximum age coeval with the Rhyacian-Orosirian tectonothermal event (Leite 2002, Spreafico 2017). These rocks lie upon the 3.4–3.2 Ga basement rocks of the northern part of the Gavião Block, composed of TTG gneiss, metagranites, and metarhyolites (Mougeot 1996, Barbosa 1997, Leal 1998, Peucat *et al.* 2002, Barbosa *et al.* 2012a, Zincone *et al.* 2016).

The Saúde Complex occurs to the east of the MNGB (Figs. 1C and 2), where the two units are in tectonic contact

Table 1. Compilation of regional geochronological data of the MNGB and surrounding units.

Geological/tectonic unit	Lithotype	Age	Method	Mineral dated	Author
Saúde Complex	Biotite schist	2068 ± 12 Ma*	U-Pb (LA-MC-ICP-MS)	Detrital zircon	Zincone *et al.* (2017)
Cachoeira Grande granite	Leucogranite	2080 ± 18 Ma	U-Pb (Electron microprobe)	Monazite (crystallization age)	Leite (2002)
Upper sequence (MNGB)	Quartzite	2133 ± 14 Ma*	U-Pb (LA-ICP-MS)	Detrital zircon	Barbuena *et al.* (2016)
Mundo Novo greenstone belt	Metadacite	2595 ± 21 Ma	U-Pb (LA-ICP-MS)	Zircon (crystallization age)	The present work
Itabuna-Salvador-Curaçá Belt	Tonalitic granulite	2574 ± 6 Ma	U-Pb (SHRIMP)	Zircon (crystallization age)	Oliveira *et al.* (2010)
	Enderbite	2695 ± 12 Ma	U-Pb (SHRIMP)	Zircon (crystallization age)	Silva *et al.* (1997)
Jequié Block	Granulites	2715 ± 29 Ma	U-Pb (SHRIMP)	Zircon (crystallization age)	Silva *et al.* (2002)
	Charnockite	2900 ± 24 Ma	Rb-Sr	Whole-rock (crystallization age)	Wilson (1987)
Serrinha Block	Granitoid	2989 ± 11 Ma 3072 ± 2 Ma 3162 ± 26 Ma	U-Pb (SHRIMP)	Zircon (crystallization age)	Rios *et al.* (2009)
	Gneiss, migmatite	3152 ± 5 Ma	U-Pb (SHRIMP)	Zircon (crystallization age)	Oliveira *et al.* (2002a, 2002b)
Jacobina Group	Quartzite	3500 - 3220 Ma	U-Pb (LA-MC-ICP-MS)	Detrital zircon	Magee *et al.* (2001); Teles (2013); Teles *et al.* (2015); Barbuena *et al.* (2016)
Mairi Block	Orthogneiss	3.33 - 3.30 Ga	U-Pb (LA-SF-ICP-MS)	Zircon (crystallization age)	Sousa *et al.* (2018)
Gavião Block	Metagranite	3291 ± 2.5 Ma	U-Pb (LA-ICP-MS)	Zircon (crystallization age)	Zincone *et al.* (2016)
	Metarhyolite	3303 ± 11 Ma 3305 ± 9 Ma	U-Pb (LA-ICP-MS and SHRIMP)	Zircon (crystallization age)	Zincone *et al.* (2016); Peucat *et al.* (2002)
	TTG	3442 ± 2 Ma	U-Pb (ID-TIMS)	Zircon (crystallization age)	Mougeot (1996)

*Youngest age.

along west-vergent thrust zones. This complex comprises aluminous paragneiss, biotite gneiss, and subordinate quartzites that are widely distributed in a north-south trend with significant occurrences in the Mundo Novo region and in the eastern portion of the Jacobina Ridge (Couto *et al.* 1978, Mascarenhas *et al.* 1998, Leite *et al.* 2007, Reis *et al.* 2017; Fig. 1C). The maximal depositional age of 2.06 Ga (Zincone *et al.* 2017) for the Saúde Complex once more indicates the presence of a sedimentary basin near the MNGB; however, the rocks in the Saúde Complex were subjected to a higher metamorphic degree than the sedimentary rocks at the top of the MNGB along the tectonic contact (Spreafico 2017, Zincone *et al.* 2017).

Finally, Rhyacian-Orosirian granites are present along the Contendas-Jacobina Lineament (Leite 2002, Spreafico 2017; Fig. 1C). In general, these granites are undeformed leucogranites, comprising quartz, feldspar, biotite, and muscovite with some occurrences of garnet and sillimanite (Barbosa *et al.* 2012b). The Cachoeira Grande granite, for example, is a peraluminous leucogranite situated to the northeast of the MNGB, which has an average age of 2080 ± 18 Ma (Leite 2002), and is coeval with the Rhyacian-Orosirian granitic intrusions in the MNGB (Spreafico 2017, Spreafico *et al.* 2018).

ANALYTICAL METHODS

The study of the metavolcanic rocks of the MNGB and considerations regarding the tectonic setting involved petrographic, mineral, and whole-rock chemistry and geochronologic analyses.

For petrography, we analyzed 127 thin sections of metakomatiite, eastern and western metabasalts and metadacite to determine the mineralogical composition and microstructures of the rocks using the ZEISS Axio Scope.A1 microscope provided by Companhia Baiana de Pesquisa Mineral (CBPM). The mineral abbreviations used on photomicrographs mainly follow those of Kretz (1983) and Siivola and Schmid (2007), and are completed with abbreviations of Whitney and Evans (2010).

Six of the thin sections were used for mineral chemistry analysis to detail the mineral differences between the two metabasalt types complementing the petrographic studies. Thus, a CAMECA SX50 electron microprobe was used with four wavelength-dispersive spectroscopes (WDS) and one Kevex energy-dispersive spectroscope (EDS) of the University of Brasília. The standards used are natural and synthetic with defined compositions, such as albite (for the element Na_2O), andradite (for the elements CaO and FeO), forsterite (for the element MgO), microcline (for the elements Al_2O_3, SiO_2, and K_2O), $MnTiO_3$ (for the element TiO_2), and $MnTiO_3$ (for the element MnO). The analyzed spots were selected in polished sections in plagioclase (6 spots in 5 samples), amphibole (6 spots in 5 samples), pyroxene (4 spots in 2 samples), ilmenite (2 spots in 2 samples), titanite (2 spots in 2 samples), and biotite (1 spot in 1 sample) grains. The chemical contents are expressed by SiO_2, TiO_2, Al_2O_3, FeO, MnO, MgO, CaO, Na_2O, and K_2O and the structural formula is provided based on cationic contents of Si, Ti, Al, Fe, Mn, Mg, Ca, Na, and K of each spot analyzed. The data were processed using the Gabbrosoft spreadsheets (http://www.gabbrosoft.org) and the plagioclase results were plotted in the ternary diagram of feldspar; the amphiboles were plotted in the calcic amphibole diagrams (Leake *et al.* 1997) and the pyroxene in the classification diagram of pyroxenes (Morimoto 1988) using the Minpet program.

The whole-rock chemical analysis of 49 samples was conducted in the SGS-Geosol laboratory. The samples were dried and crushed so 75% of the sample was smaller than 3 mm. A 300 g sample was quartered and pulverized (until 95% was smaller than 105 microns) to form a powder for subsequent processes. The powders were melted at a high temperature with lithium metaborate, and the major, minor, trace, and rare earth elements (REE) were determined using ICP-MS and inductively coupled plasma optical emission spectrometry (ICP-OES) analysis. The international standard samples used are TILL-3 (description and values are in Lynch 1996) and GRE-05 (reference material from Geostats PTY Ltd.). The error for all analyzed elements in each sample was calculated based on analytical accuracy according to the content of the analyte in the sample, the statistical detection (Supplementary Data) and repeatability limits, and represented in terms of standard deviation (1σ) (Thompson 1988). The coefficient of variation of the analytical results for each element by sample analyzed, calculated from the standard deviation (1σ), was predominantly lower than 15%, which corresponds to well-represented results around the arithmetic mean. Only the samples with a loss on ignition (LOI) values of ≤ 5% were considered. The geochemical data were plotted and interpreted using the GCDKit software (Janousek *et al.* 2006). The data in the REE diagram and the $(La/Yb)_N$, $(Gd/Yb)_N$ and Eu/Eu* ratios were normalized by chondrite values (Boynton 1984), and the data in the multielement diagram were normalized by N (normal)-MORB values (Hofmann 1988).

The U-Pb geochronologic analyses of one metadacite sample were conducted at the Center of Geochronology Research at the Institute of Geosciences, University of São Paulo. The zircon grains from the sample were separated using binocular microscopy and placed in a 2.5 cm epoxy support. Then, the zircons were polished with sandpaper, and photomicrographs were captured. The internal structures of the zircon grains were characterized using cathodoluminescence (CL) images obtained by a FEI Quanta 250 scanning electron microscope (SEM) and a XMAX CL detector (Oxford Instruments), and the analysis was acquired using in situ LA-ICP-MS. The analysis was performed with a Neptune (Thermo) multicollector instrument and an ArF-193 nm Photon laser system (frequency of 6 Hz) with a spot diameter of 32 μm. The final results match the average obtained after calculating two standard deviations. Isotopic ratios are reported at level 1σ. Finally, the discordant values for the zircon data greater than 10% were eliminated. Corrections for the laser-induced elemental fractionation of the $^{206}Pb/^{238}U$ ratio and instrumental discrimination were based on the GJ-1 zircon standard (U-Pb mean age of 601 ± 3.5 Ma; Elhlou

et al., 2006), which yielded an age of 600.7 ± 0.69 Ma in the analyzed period. The raw data were processed online and reduced in an Excel spreadsheet adapted from SQUID 1.02 (Ludwig 2001). The data were plotted on a concordia diagram using ISOPLOT/Ex®3.00 (Ludwig 2003).

GEOLOGICAL, PETROGRAPHIC, AND MINERAL CHEMISTRY CHARACTERIZATION

The MNGB metavolcanic rocks occur into two stratigraphic sequences: in the *lower sequence*, which is composed of metakomatiite; and in the *middle sequence*, which is composed of eastern and western metabasalts and, subordinately, tremolitite, calc-silicate rock (carbonate hydrothermal alteration zone), aluminous schist (argilic-chloritic hydrothermal alteration zone), BIF, ferruginous metachert, metadacite, and metarhyolite (Fig. 2).

Lower sequence

The lower sequence is composed of metakomatiite located at the base of the MNGB and comprises the ultramafic volcanic component of the MNGB. The metakomatiite has field relationships with the mafic volcanic rock of the middle sequence; however, these rocks are separated into different sequences due to the mineral content and the microstructural particularities. There are four restricted occurrences of metakomatiite in the central portion of the MNGB, which are northeast of Mundo Novo city and northeast of Piritiba city (Fig. 2).

Generally, the metakomatiite of the MNGB has a relict spinifex microstructure composed of skeletal grains with planar growths that intersect each other (Figs. 3A and 4A) and do not intercept former structures for igneous relicts' microstructure in komatiites, as described by Arndt (1994). The fine-grained spinifex microstructure is identified only in hand samples or by using a hand lens or microscope.

The metakomatiite of the MNGB has a light green color, a silky aspect, and is not magnetic (Fig. 3A). The rock is isotropic and the olivine and pyroxene crystals are entirely replaced by acicular and prismatic pseudomorphic grains of anthophyllite and tremolite (75–80% of the rock) with a grain size of 0.5 mm (Tab. 2; Fig. 4A). The fine-grained groundmass is composed of talc and clinochlore (20–25% of the rock) without a preferred orientation. Traces of pyrite and pyrrhotite are dispersed in the samples.

Middle sequence

The middle sequence is composed of metabasalt and, subordinately, tremolitite, calc-silicate rock, aluminous schist, BIF, ferruginous metachert, metadacite and subordinate metarhyolite; metabasalt and metadacite are the main topics of this study.

Metabasalt and metadacite are the terms used in this paper to define the mafic and felsic volcanic components, respectively, of the middle sequence of the MNGB. These terminologies were adopted based on the respective protolith due to its usefulness in determining the original nature of the rock, even though in many cases, a protolith name does not reflect the principal minerals and structural features of the rocks under observation (Schmid *et al.* 2007). Moreover, some occurrences of metavolcanic mafic rocks in the MNGB preserve primary structures such as pillow lava. Therefore, the term metabasalt is mainly used in this manuscript rather than amphibolite, which is also correctly used if the microstructure and mineral content are considered as proposed by Fettes *et al.* (2007).

The metabasalts are distributed along a north-south trend (Fig. 2) and are divided into two coeval groups based

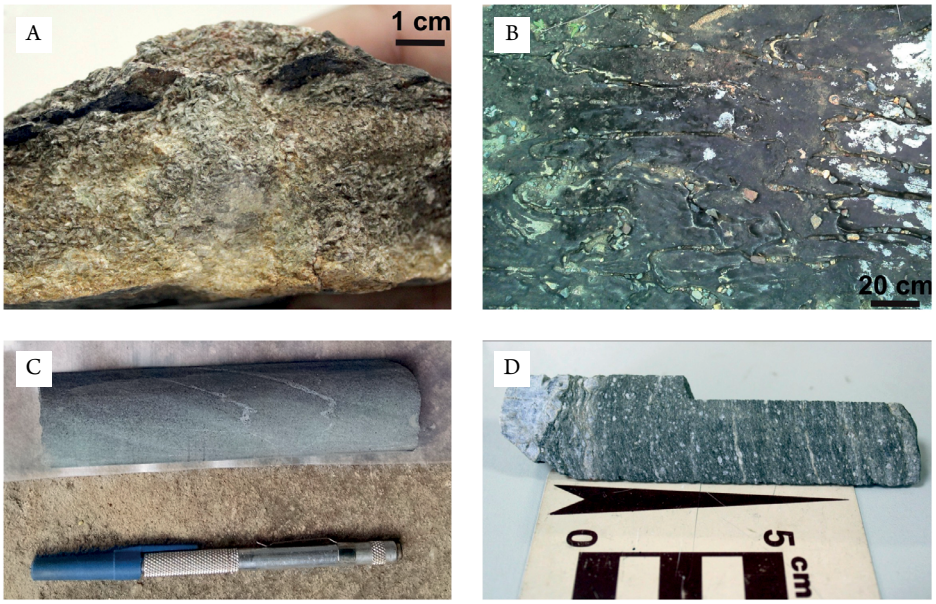

Figure 3. (A) Relict fine-grained spinifex microstructure of the MNGB metakomatiite (sample FD-058A; W. Long.: 40º28'45.53" S. Lat.: 11º41'43.47", Datum: SIRGAS 2000). (B) Highlighted pillow lava structure of the aphanitic and equigranular eastern metabasalt from south of the MNGB (sample RR-018A; W. Long.: 40º30'07.88" S. Lat.: 12º13'43.29"). (C) Drill hole sample of the aphanitic and inequigranular western metabasalt in the MNGB (sample RR-F6-001; W. Long.: 40º29'35.54" S. Lat.: 11º53'35.26"). (D) Drill hole sample of the fine-grained porphyroclastic metadacite in the MNGB (sample FD-052; W. Long.: 40º29'26.72" S. Lat.: 11º42'09.52").

on petrography, supported by mineral chemistry analysis, and whole-rock chemical data. The first group, defined as the eastern metabasalt, occurs along the eastern portion of the MNGB, has field relationships with the metakomatiite of the lower sequence and corresponds to the main outcrops of the sequence near Piritiba city and extending to Ruy Barbosa city (Fig. 2). The second group, defined as the western metabasalt, occurs along the western portion of the MNGB, mainly within the Fazenda Coqueiro deposit (Mundo Novo city), and in a restricted area with a north-south trend near Piritiba city (Fig. 2).

Eastern metabasalt

The eastern metabasalt has a dark green to dark grey color and preserves the pillow lava structures that occur in a large area to the south of the MNGB (Fig. 3B). It is composed of anorthite (15–20%), bytownite (10–15%), magnesiohornblende and ferrohornblende (35–40%), small amounts of oligoclase (5–10%), and low percentages (15–20% combined) of augite, edenite and quartz, as well as ilmenite and titanite as accessory minerals, and traces of pyrrhotite, chalcopyrite, and igneous relicts of hypersthene micrograins identified only in microprobe analyses (5–10%; Tab. 2 and 3; Figs. 5A, 5B, 5C and 5D). The rock is

Table 2. Modal mineral composition of metavolcanic rocks of the lower (metakomatiite) and middle (eastern and western metabasalts, metadacite and metarhyolite) sequences of the MNGB.

Geologic unit	**Metakomatiite**	**Eastern metabasalt**	**Western metabasalt**	**Metadacite**	**Metarhyolite**
Characteristics	**Acicular and prismatic pseudomorphic grains and fine-grained groundmass**	**Equigranular and aphanitic with granonematoblastic microstructures**	**Inequigranular, aphanitic with schistosity planes**	**Fine-grained porphyroclastic microstructure**	**Fine-grained porphyroclastic microstructure**
Minerals, vol.%					
Quartz	-	5–7	3–5	27.5–31.8	20–25
Anorthite	-	15–20	-	-	-
Bytownite	-	10–15	-	-	-
Andesine		-	25–27.5	-	-
Oligoclase	-	5–10	25–27.5	-	-
Plagioclase	-	-	-	27.5–31.8	15–20
K-Feldspar	-	-	-	10–10.8	40–45
Biotite	-	-	5–7	10–10.8	10–15
Muscovite	-	-	-	10–10.8	-
Sericite	-	-	-	10–10.8	3–7
Fe-Hornblende + Mg-Hornblende	-	35–40	-	-	-
Fe-Tschermakite + Mg-Hornblenda	-	-	17–20	-	-
Actinolite	-	-	8–10	-	-
Anthophyllite + Tremolite	75–80	-	-	-	-
Edenite	-	5–7	-	-	-
Augite	-	5–6		-	-
Hypersthene	-	3–4	2–3	-	-
Talc + Clinochlore	20–25	-	-	-	-
Pyrite	-	-	Tr	-	-
Pyrrhotite	-	Tr	Tr	-	-
Chalcopyrite	-	Tr	Tr	-	-
Galena	-	-	Tr	-	-
Sphalerite	-	-	Tr	-	-
Arsenopyrite	-	-	Tr	-	-
Titanite	-	2–3	2.5–5	-	-
Ilmenite	-	2–3	2.5–5	Tr	Tr
Mn-Ilmenite	-	-	Tr	-	-
Zircon	-	-	-	Tr	Tr
Sum, vol.%	100	100	100	100	100

Tr: Trace concentration.

isotropic, equigranular, and aphanitic, it has nematoblastic to granonematoblastic microstructures, and the minerals show polygonal contacts (Fig. 4B).

Western metabasalt

The western metabasalt has a green to grey color and hosts the Zn and Pb sulfides of the Fazenda Coqueiro deposit, particularly in carbonate hydrothermal alteration zones, and is easily observed from drill hole samples obtained by CBPM (Fig. 3C). Based on petrography and mineral chemistry results, this rock is very fine-grained and is mainly composed of oligoclase and andesine (50–55%), actinolite, magnesiohornblende, and ferrotschermakite (25–30%) with a low percentage of quartz, biotite and igneous relicts of hypersthene micrograins (10–15%), as well as ilmenite and titanite as accessory minerals (5–10%; Tab. 2 and 3; Figs. 5A, 5B, 5C and 5D). Traces of manganiferous ilmenite, pyrrhotite, pyrite, chalcopyrite, galena, sphalerite, and arsenopyrite are also observed. The rock is anisotropic, inequigranular and aphanitic, has a polygonal granonematoblastic microstructure and the grains of biotite and actinolite are oriented defining schistosity planes (Fig. 4C).

Metadacite and subordinate metarhyolite

These rocks have restricted occurrences and correspond to the top of the MNGB middle sequence based on field relationships and on a felsic mineral content typical of the later stages of volcanism. These units occur to the northeast of Piritiba city and were identified in drill hole samples and in outcrops (Fig. 2). These rocks are distributed along a northeast-southwest trend and are in contact with eastern metabasalt and ferruginous metachert (Fig. 2).

The metadacite is gray colored, it has a porphyroclastic microstructure, and is not magnetic. This rock contains submillimetric porphyroclasts of plagioclase with sericitized borders and quartz (35–40% of the rock), dispersed in a fine-grained groundmass composed of quartz, plagioclase, K-feldspar, biotite, muscovite, and sericite (60–65% of the rock; Tab. 2; Figs. 3D and 4D), and traces of zircon and other opaque minerals.

The subordinate metarhyolite is gray in color and has a fine-grained porphyroclastic microstructure. It is composed of quartz (20–25%), K-feldspar (40–45%), plagioclase (15–20%), biotite (10–15%), and sericite (3–7%; Tab. 2). This rock contains phyllosilicate grains that are submillimetric and highly oriented, tabular crystals of plagioclase (usually sericitized) and grains of quartz, fine biotite and opaque minerals.

U-PB GEOCHRONOLOGY IN ZIRCON

For LA-ICP-MS U-Pb zircon age determination, the metadacite (sample FD-052) of the middle sequence was selected (see sample site in Figs. 1 and 2).

Zircons in the metadacite sample FD-052 are light to dark brown, translucent, subhedral, and prismatic with subrounded terminations. Grain lengths range from 77 to 550 µm, and the aspect ratios range from 2.0 to 3.0. Some crystals show concentric oscillatory zoning and some unzoned ones. Generally, the zircons present thin metamorphic rims and resorbed portions. Twenty-four analyses (Tab. 4) were performed in the cores,

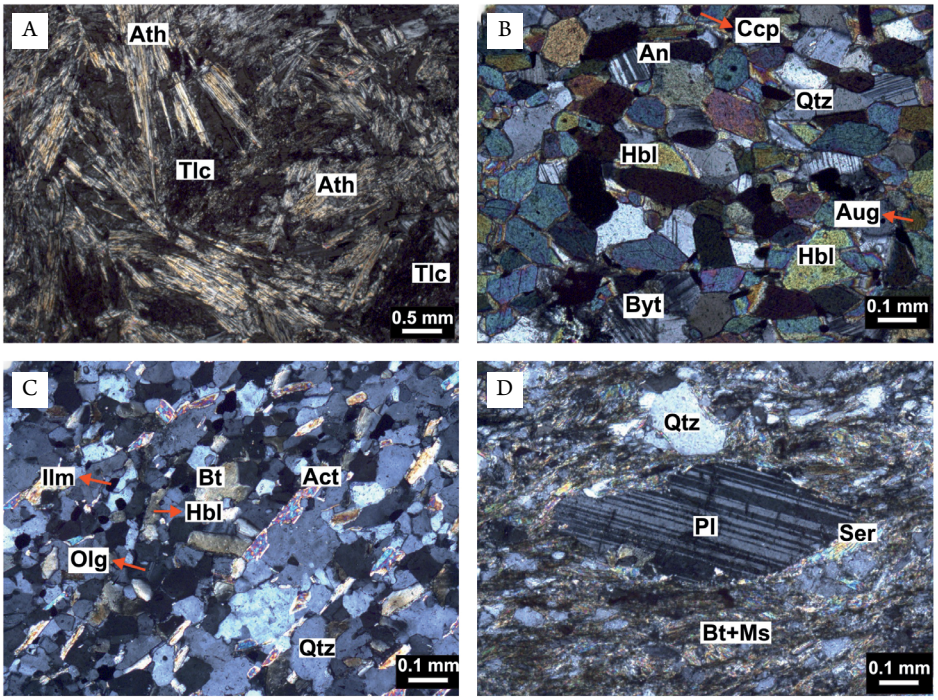

Mineral abbreviations: Act: actinolite; An: anorthite; Ath: anthophyllite; Aug: augite; Bt: biotite; Byt: Bytownite; Ccp: chalcopyrite; Hbl: hornblende; Ilm: ilmenite; Ms: muscovite; Olg: oligoclase; Pl: plagioclase; Qtz: quartz; Ser: sericite; Tlc: talc.

Figure 4. Petrographic images of the MNGB: (A) Relict spinifex microstructure of metakomatiite composed of pseudomorphic anthophyllite lath in a fine-grained groundmass of talc (sample FD-058A; W. Long.: 40°28'45.53" S. Lat.: 11°41'43.47°. Datum: SIRGAS 2000). (B) Polygonal granonematoblastic microstructure of the eastern metabasalt (sample RR-018A; W. Long.: 40°30'07.88" S. Lat.: 12°13'43.29"). (C) Typical very fine-grained and polygonal granonematoblastic microstructure of the western metabasalt (sample RR-F6-001; W. Long.: 40°29'35.54" S. Lat.: 11°53'35.26"). (D) Porphyroclast of plagioclase with a sericitized border in a fine-grained groundmass of quartz, biotite, and muscovite in the metadacite in the middle sequence of the MNGB (sample FD-052; W. Long.: 40°29'26.72" S. Lat.: 11°42'09.52").

Table 3. Electron microprobe data of the oxides of the elements analyzed reported in wt.% and the cationic structural formula of the minerals in the eastern and western metabasalts.

Geologic unit	Sample ID	Mineral	SiO_2	TiO_2	Al_2O_3	FeO	MnO	MgO	CaO	Na_2O	K_2O	Sum
Eastern metabasalt	RR-072	Anorthite	46.60	0.08	35.37	0.29		0.01	18.41	1.17	0.03	101.96
Eastern metabasalt	RR-072	Anorthite	46.15		35.53	0.38		0.01	18.34	1.09	0.02	101.52
Eastern metabasalt	RR-018A	Bytownite	49.26	0.08	32.93	0.16	0.11	0.02	15.80	2.56	0.10	101.02
Eastern metabasalt	RR-011C	Oligoclase	62.40		22.79	0.09			3.50	9.20	0.08	98.06
Eastern metabasalt	RR-072	Fe-Hornblende	44.13	0.30	14.20	17.28	0.19	8.92	11.76	1.08	0.24	98.1
Eastern metabasalt	RR-011C	Mg-Hornblende	48.25	0.12	7.27	12.51	0.24	14.27	11.07	1.53	0.14	95.40
Eastern metabasalt	RR-018A	Edenite	51.46	0.18	0.62	14.97	0.41	9.19	22.71	0.16	0.01	99.71
Eastern metabasalt	RR-072	Hypersthene	53.07	0.19	0.55	25.94	0.60	15.04	0.93	0.06		96.38
Eastern metabasalt	RR-072	Hypersthene	52.59	0.04	1.00	26.40	0.56	15.07	1.40	0.08		97.14
Eastern metabasalt	RR-072	Hypersthene	52.77	0.18	0.40	26.53	0.74	15.14	0.86	0.07		96.69
Eastern metabasalt	RR-072	Titanite	16.79	42.49	1.06	25.39	0.66	0.70	14.00	0.03		101.12
Eastern metabasalt	RR-072	Ilmenite	0.10	50.58	0.03	45.84	0.79	0.07	0.02	0.03	0.01	97.47
Western metabasalt	RR-F6-001	Oligoclase	59.95	0.23	23.20	0.04			5.09	8.71	0.04	97.26
Western metabasalt	RR-F6-010	Andesine	56.79	0.03	26.89	0.14			9.04	6.45	0.05	99.39
Western metabasalt	RR-F1-001	Mg-Hornblende	46.43	0.67	8.44	18.06	0.42	10.09	11.7	0.90	0.38	97.09
Western metabasalt	RR-F1-001	Fe-Tschermakite	40.86	0.88	11.69	27.16	0.33	3.85	11.67	0.92	1.13	98.49
Western metabasalt	RR-F6-010	Fe-Tschermakite	41.31	0.89	11.28	26.92	0.37	3.91	11.58	1.03	1.06	98.35
Western metabasalt	RR-F6-001	Hypersthene	51.63	0.07	0.86	27.03	0.66	15.62	0.73	0.13		96.73
Western metabasalt	RR-F1-001	Biotite	33.06	2.45	15.68	28.96	0.33	4.86	0.04	0.16	9.46	95.00
Western metabasalt	RR-F1-001	Titanite	29.95	36.06	2.29	1.99	0.09	0.24	26.69	0.02	0.41	97.74
Western metabasalt	RR-F6-001	Ilmenite		54.86		46.66	2.32	0.06	0.07		0.01	103.98

Structural formula of the minerals:

Geologic unit	Sample ID	Mineral	Si	Ti	Al	Fe	Mn	Mg	Ca	Na	K	Sum
Eastern metabasalt	RR-072	Anorthite	2.106	0.003	1.884	0.011		0.001	0.891	0.103	0.002	5.001
Eastern metabasalt	RR-072	Anorthite	2.095		1.901	0.014		0.001	0.892	0.096	0.001	5.000
Eastern metabasalt	RR-018A	Bytownite	2.231	0.003	1.758	0.006	0.004	0.001	0.767	0.225	0.006	5.001
Eastern metabasalt	RR-011C	Oligoclase	2.810		1.210	0.003			0.169	0.803	0.005	5.000
Eastern metabasalt	RR-072	Fe-Hornblende	6.526	0.033	2.475	2.137	0.024	1.967	1.863	0.310	0.045	17.380*
Eastern metabasalt	RR-011C	Mg-Hornblende	7.164	0.013	1.272	1.553	0.030	3.159	1.761	0.440	0.027	17.420*
Eastern metabasalt	RR-018A	Edenite	7.619	0.020	0.108	1.854	0.051	2.028	3.603	0.046	0.002	17.331*
Eastern metabasalt	RR-072	Hypersthene	2.080	0.006	0.025	0.850	0.020	0.879	0.039	0.005		3.904
Eastern metabasalt	RR-072	Hypersthene	2.054	0.001	0.046	0.862	0.019	0.878	0.059	0.006		3.925
Eastern metabasalt	RR-072	Hypersthene	2.071	0.005	0.018	0.871	0.025	0.886	0.036	0.005		3.917
Eastern metabasalt	RR-072	Titanite	0.612	1.164	0.046	0.774	0.020	0.038	0.546	0.002		3.202
Eastern metabasalt	RR-072	Ilmenite	0.006	1.976	0.002	1.992	0.034	0.006	0.002	0.004		4.022
Western metabasalt	RR-F6-001	Oligoclase	2.728	0.008	1.244	0.002			0.248	0.768	0.002	5.000
Western metabasalt	RR-F6-010	Andesine	2.561	0.001	1.429	0.005			0.437	0.564	0.003	5.000
Western metabasalt	RR-F1-001	Mg-Hornblende	6.982	0.076	1.496	2.271	0.053	2.262	1.885	0.262	0.073	17.362*
Western metabasalt	RR-F1-001	Fe-Tschermakite	6.412	0.104	2.162	3.565	0.044	0.901	1.962	0.280	0.226	17.656*
Western metabasalt	RR-F6-010	Fe-Tschermakite	6.479	0.105	2.085	3.531	0.049	0.914	1.946	0.313	0.212	17.634*
Western metabasalt	RR-F6-001	Hypersthene	2.035	0.002	0.040	0.891	0.022	0.918	0.031	0.010		3.949
Western metabasalt	RR-F1-001	Biotite	2.684	0.150	1.500	1.966	0.023	0.588	0.003	0.025	0.980	9.919*
Western metabasalt	RR-F1-001	Titanite	1.004	0.909	0.090	0.056	0.003	0.012	0.958	0.001	0.018	3.051
Western metabasalt	RR-F6-001	Ilmenite		2.002		1.893	0.095	0.004	0.004			3.998

*For amphibole and biotite were added 2.0 atomic units of H_2O. The structural formula for the feldspar was provided based on 8 oxygens, for the amphibole based on 23 oxygens, for the hypersthene based on 6 oxygens, for the biotite based on 11 oxygens, for the titanite based on 5 oxygens and for the ilmenite based on 6 oxygens.

and the results define the crystallization age. The data in the concordia diagram yield an upper intercept age of 2595 ± 21 Ma, and the MSWD = 2.3 (Fig. 6); thus, this age is considered to represent crystallization age. These data present concordances of between 55 and 91%, and the Th/U values range from 0.31 to 1.03 (values of igneous zircons). The lower intercept age of 616 ± 25 Ma indicates a loss of Pb, possibly from low-intensity geological processes.

GEOCHEMICAL CHARACTERIZATION

The bivariate diagrams of TiO_2 and Al_2O_3 (the least mobile major elements), FeO_t and MgO (mobile major elements), Ni (conservative trace element), Y (immobile trace element), and La and Ce (light REE) against Zr were drawn for the metakomatiite from the lower sequence and the eastern and western metabasalts and metadacite from the middle sequence of the MNGB; the diagrams are shown in Figure 7, and show important correlations. Zr was used as a crystal fractionation index due to its immobility during alteration and metamorphism and its large range of concentration in igneous suites, resulting from varying degrees of partial melting and fractional crystallization (Furnes *et al.* 2013).

TiO_2 defines a positive pattern *versus* Zr, and the eastern and western metabasalts form separate groups with the same slope. The Al_2O_3 diagram features a positive asymptotic pattern, in which the metakomatiite samples plot near the origin, the metabasalt samples form a trend where the western metabasalt exhibits relatively high values of Al_2O_3, and the metadacite is approximately aligned in the trend. Four distinct and dispersed groups are formed in the FeO_t plot, possibly due to the mobility of Fe during the alteration. The negative asymptotic patterns in the MgO and Ni diagrams form highly defined trends that can be explained by the fractional crystallization of olivine and pyroxene in the metakomatiite and eastern and western metabasalts. Y, La, and Ce, which are considered immobile elements, show highly defined positive correlations *versus* Zr. Therefore, they were used to demonstrate that metakomatiite, eastern and western metabasalts, and metadacite from the MNGB can be related by fractional crystallization.

Lower sequence

The metakomatiite of the MNGB is ultramafic, with MgO concentrations of 17-25 wt.% (Tab. 5; Fig. 8A). The chondrite-normalized REE geochemical pattern (Boynton 1984) indicates enrichment in light REE in the metakomatiite in the MNGB, similar to the komatiite pattern from the Onverwacht Suite of the Barberton greenstone belt, South Africa (Jahn *et al.* 1982; Tab. 6; Fig. 8D). The pattern of distribution of elements

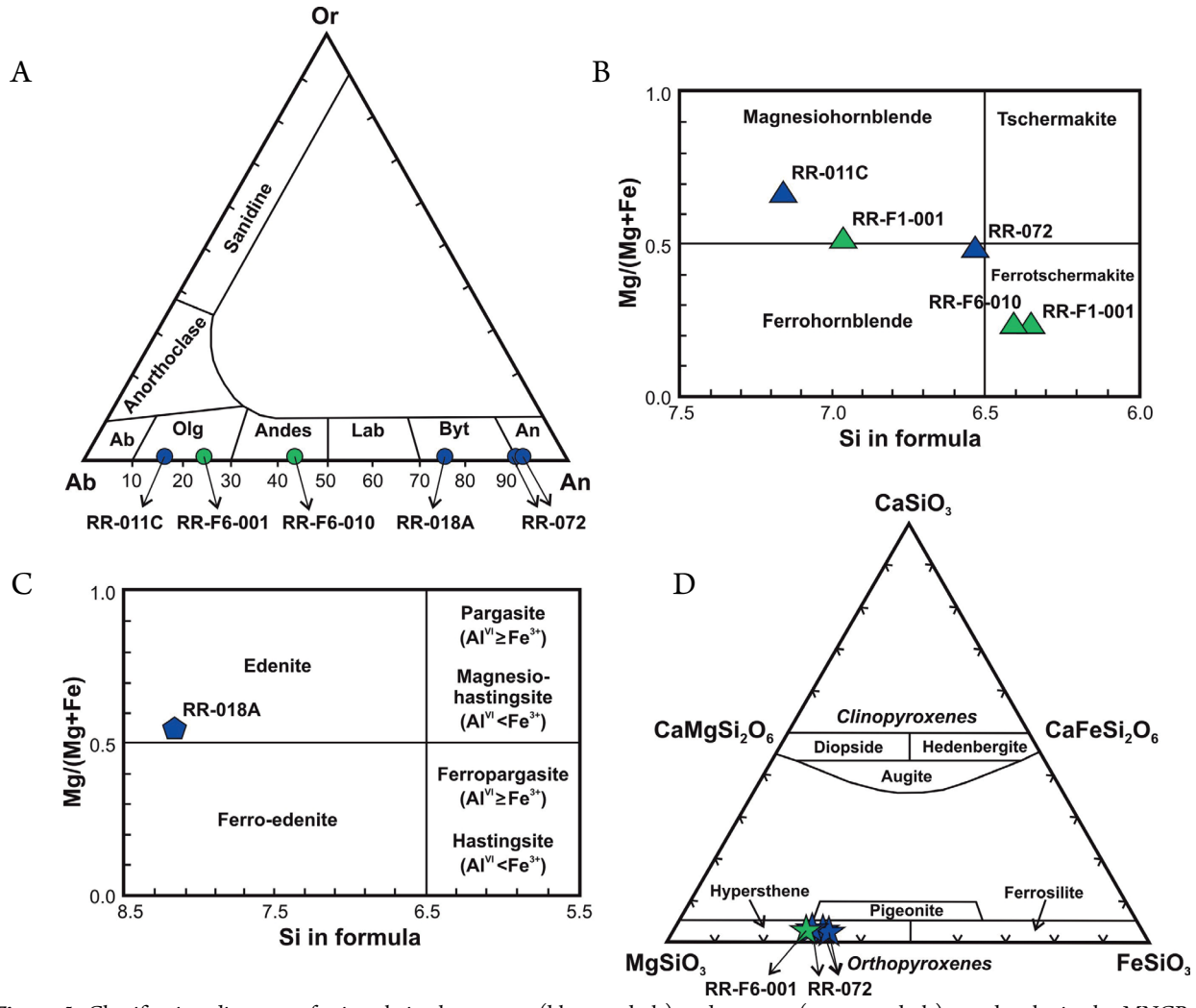

Figure 5. Classification diagrams of minerals in the eastern (blue symbols) and western (green symbols) metabasalts in the MNGB. (A) Ternary diagram of feldspar: Ab: albite; Andes: andesine; An: anorthite; Byt: bytownite; Lab: labradorite; Olg: oligoclase; Or: orthoclase. (B and C) Classification diagrams of the calcic amphiboles (Leake *et al.* 1997). (D) Classification diagram of pyroxenes (Morimoto 1988).

resulted from low values of Nb (≤ 2.45 ppm) and Ti (≤ 1500 ppm), in addition to the enrichment in U and Th (Tab. 7) can be observed in Fig. 9A. High CaO/Al_2O_3 ratios (Herzberg 1995) in the metakomatiite of the MNGB, with three samples greater than 1.10 (Tab. 8), allow this rock to be classified as Al-depleted.

The $(La/Yb)_N$ ratios in the MNGB's metakomatiite show high values, with an average of approximately 6.79, standard deviation (σ) of 4.21 and a minimum value of 3.00, and the $(Gd/Yb)_N$ ratios values show an average of 1.34 (σ = 0.21) and a minimum of 1.09 (Tab. 6 and 8). The Eu/Eu* ratios values for the metakomatiite have an average of 0.95 (σ = 0.06), suggesting a subtle negative europium anomaly (Tab. 8). The Ce/Ce* ratios show values around 3.72 and the ΣREE indicates an average of 29.32 ppm (σ = 5.33, Tab. 6 and 8).

Table 4. U-Pb geochronological data, sample FD-052: metadacite from the middle sequence of the MNGB (2595 ± 21).

Spot name	U (ppm)	Th	Th/U	Pb_{com}	$^{207}Pb/$	1σ	$^{207}Pb/$	1σ	$^{206}Pb/$	1σ	$^{207}Pb/^{206}Pb$	1σ	%Conc.	Error cor.
	ppm	ppm			^{206}Pb		^{235}U		^{238}U		age (Ma)			
1.1	658.4	275.8	0.419	1.25	2.6011	0.1320	0.1667	0.0049	5.9986	0.1771	1.851	0.063	53	0.98
2.1	616.1	277.4	0.450	2.53	3.2253	0.1528	0.1887	0.0056	5.2998	0.1561	2.014	0.061	55	0.92
3.1	101.7	43.7	0.430	0.42	10.4939	0.4770	0.4391	0.0133	2.2776	0.0692	2.590	0.050	90	0.78
4.1	728.8	408	0.560	1.90	1.5881	0.0810	0.1275	0.0038	7.8457	0.2310	1.433	0.077	53	0.96
5.1	452.6	253.4	0.560	4.34	6.1109	0.2648	0.2899	0.0081	3.4494	0.0968	2.378	0.052	69	0.99
6.1	599	298	0.498	0.09	2.3350	0.1107	0.1497	0.0044	6.6794	0.1945	1.850	0.064	48	0.98
7.1	385.1	164.7	0.428	0.37	4.3756	0.1945	0.2258	0.0064	4.4288	0.1246	2.234	0.057	58	0.99
8.1	415.9	198.2	0.477	0.08	2.2921	0.1151	0.1508	0.0045	6.6297	0.1965	1.803	0.067	50	0.97
9.1	372.7	152.8	0.410	0.05	4.2641	0.1927	0.2212	0.0064	4.5215	0.1312	2.225	0.056	57	0.97
10.1	283.1	113.6	0.401	0.04	7.3544	0.3155	0.3365	0.0094	2.9720	0.0830	2.440	0.052	76	0.90
11.1	388	156.1	0.402	0.78	4.5986	0.2045	0.2332	0.0066	4.2885	0.1216	2.264	0.055	59	0.98
12.1	450.1	205.3	0.456	0.55	2.3444	0.1156	0.1531	0.0045	6.5328	0.1934	1.817	0.066	50	0.98
13.1	406.3	160.6	0.395	0.06	3.4443	0.1674	0.1995	0.0061	5.0133	0.1540	2.032	0.062	57	0.49
14.1	193.1	73.7	0.382	0.21	8.2819	0.3658	0.3638	0.0109	2.7491	0.0827	2.509	0.055	79	0.35
15.1	329.7	128.6	0.390	0.18	6.6123	0.3050	0.3032	0.0094	3.2986	0.1025	2.436	0.055	70	0.99
16.1	300.9	113.2	0.376	0.31	8.5090	0.3625	0.3804	0.0109	2.6287	0.0750	2.479	0.055	83	0.98
17.1	351.1	182.4	0.520	0.13	5.6869	0.2459	0.2766	0.0082	3.6159	0.1069	2.336	0.058	67	0.87
18.1	327.6	171.5	0.524	0.49	4.0965	0.1937	0.2147	0.0068	4.6585	0.1467	2.207	0.064	56	0.88
19.1	435.1	203.3	0.467	0.37	2.9071	0.1374	0.1726	0.0054	5.7929	0.1824	1.988	0.063	51	0.97
20.1	618.3	339.5	0.549	0.04	1.6806	0.0784	0.1288	0.0039	7.7629	0.2344	1.520	0.070	51	0.97
21.1	242.3	75	0.310	0.51	7.0616	0.3039	0.3297	0.0095	3.0326	0.0878	2.405	0.056	76	0.88
22.1	480.2	204.1	0.425	0.54	2.5025	0.1152	0.1625	0.0049	6.1542	0.1866	1.827	0.066	53	0.87
23.1	585.9	291.2	0.497	0.38	1.6196	0.0764	0.1275	0.0038	7.8418	0.2358	1.470	0.072	52	0.97
24.1	452.8	467	1.031	0.28	4.5256	0.2037	0.2310	0.0069	4.3296	0.1303	2.253	0.058	59	0.99

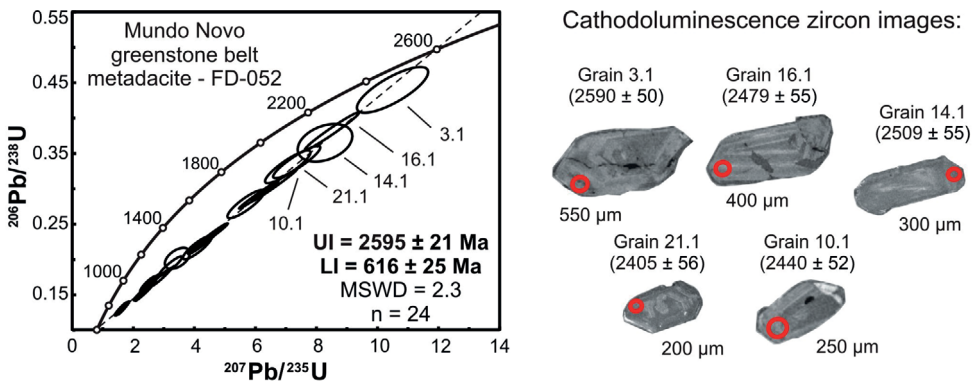

UI: upper intercept, LI: lower intercept.

Figure 6. U-Pb concordia diagram of the LA-ICP-MS data for the metadacite of the MNGB: crystallization age of 2595 ± 21 Ma. Circles in the cathodoluminescence zircon images represent the spot size; the ages are reported in million years and the lengths are reported for each grain separately.

In the multielement diagram normalized to N-MORB (Hofmann 1988), the Cs, Ba, Th and U elements show high and anomalous concentrations in the metakomatiite as compared to the other elements in the diagram, a flat pattern from Lu to Nd and a negative anomaly of Nb as compared to the neighboring elements in the diagram of the Fig. 9A.

The tectonic setting discrimination diagram of immobile elements, the Nb/Yb-Th/Yb diagram, indicates that the metakomatiite plots form a trend with other mafic volcanic rocks of the MNGB which extends from the N-MORB point to the volcanic arc array (Fig. 9E).

Middle sequence

Eastern and western metabasalts

The division of MNGB metabasalt into the two eastern and western groups, as previously discussed based on petrography, was further confirmed by the REE patterns. These patterns are reliable because of the immobility of such elements during low-grade metamorphism, weathering and hydrothermal alteration, and therefore, a degree of confidence can be placed in the obtained patterns (Rollinson 1993).

The two groups have subtle differences. The eastern metabasalt is high-iron tholeiitic, showing higher percentages of Fe and Ti than the western metabasalt (Fig. 8A), which suggests a small andesitic trend starting from the tholeiitic field in some western metabasalt samples. In the AFM diagram (Irvine and Baragar 1971), two distinct groups of samples are also present, both in the tholeiitic series field, with just three samples of the western metabasalt plotting in the calc-alkalic series field (Fig. 8B).

In the chondrite-normalized REE diagram (Boynton 1984), the western metabasalt is more fractionated and enriched in light rare earth elements (LREE) than the eastern metabasalt, which shows a flat REE pattern (Tab. 6; Figs. 8E and 8F). The fractionation difference is also observed in the average $(La/Yb)_N$ ratio: the western metabasalt has a value of 4.47 and the eastern one has a value of 1.91 (Tab. 8). The $(Gd/Yb)_N$ ratios show

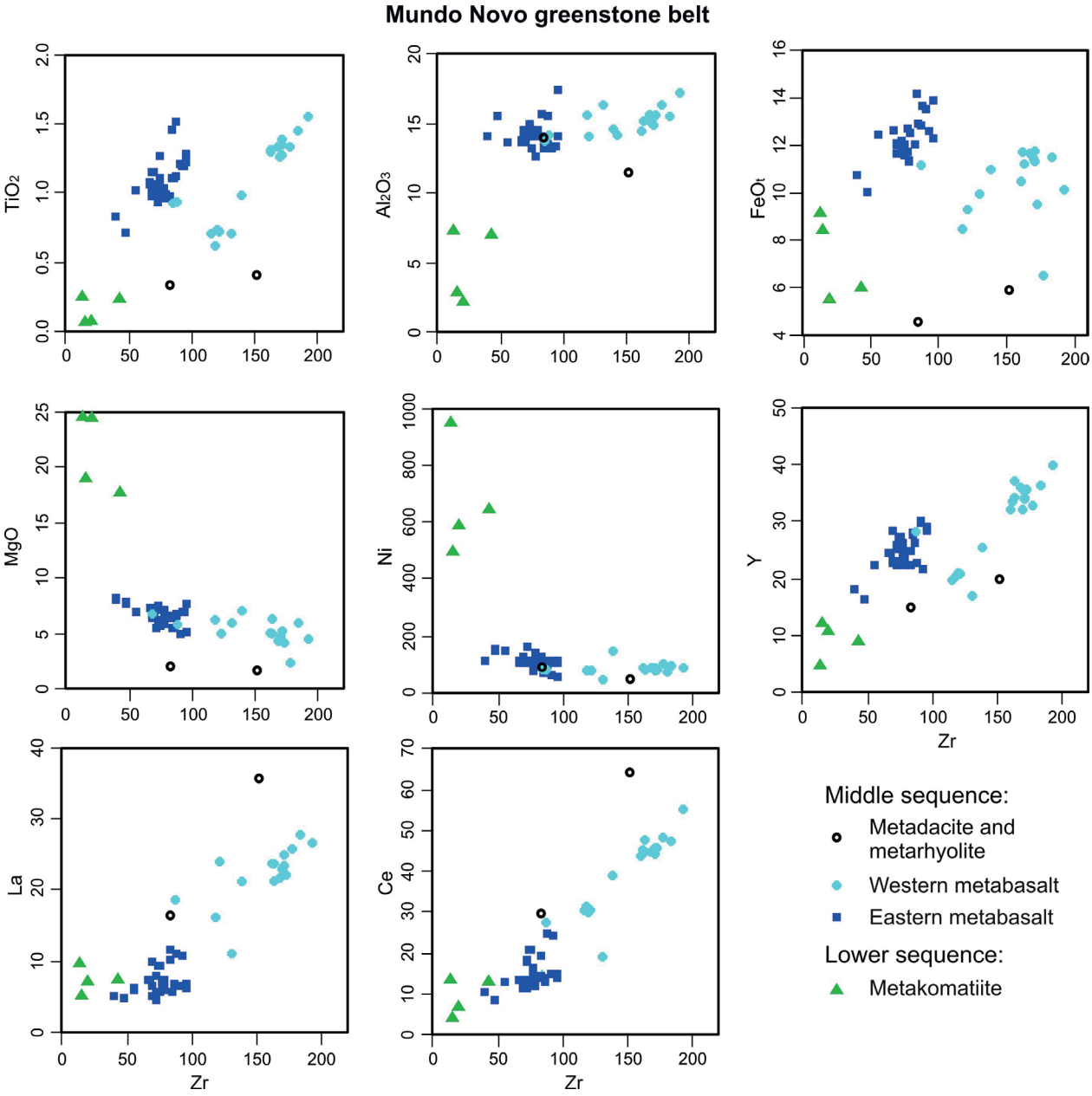

Figure 7. Binary plots using Zr as a differentiation index for the metavolcanic rocks of the MNGB.

Table 5. Whole-rock major and minor oxide chemical data (wt.%)*.

Unit and classification	Sample ID	W. Long.	S. Lat.	SiO_2	TiO_2	Al_2O_3	Fe_2O_3t	MnO	MgO	CaO	Na_2O	K_2O	P_2O_5	LOI	Sum
Mundo Novo greenstone belt															
Metakomatiite	RR-011B	40°25'02.20"	11°48'39.22"	47.01	0.25	7.33	10.18	0.22	24.46	2.99	0.08	0.03	0.005	5.49	98.05
Metakomatiite	FD-37-017	40°30'22.03"	11°41'07.33"	54.39	0.23	7.12	6.68	0.65	17.57	10.15	0.65	0.3	0.19	3.73	101.66
Metakomatiite	FD-058A	40°28'45.53"	11°41'43.47"	57.22	0.07	2.19	6.12	0.11	24.38	2.42	0.05	0.03	0.005	4.52	97.12
Metakomatiite	FD-070	40°28'36.03"	11°41'39.19"	55.02	0.07	2.81	9.38	0.23	18.91	7.4	0.11	0.03	0.005	4.03	98.00
Eastern metabasalt	RR-006	40°25'40.85"	11°53'04.26"	49.78	0.83	14.05	11.97	0.21	8.1	12.53	0.96	0.25	0.04	0.55	99.27
Eastern metabasalt	RR-011C	40°25'02.20"	11°48'39.22"	49.08	1.19	13.39	14.03	0.24	6.98	10.67	0.8	0.32	0.05	0.8	97.55
Eastern metabasalt	RR-014B	40°30'21.91"	11°41'40.20"	50.49	1	13.71	13.42	0.22	6.33	10.69	2.2	0.26	0.06	1.22	99.60
Eastern metabasalt	RR-018A	40°30'07.88"	12°13'43.29"	48.93	1.04	14.18	14.11	0.23	7.16	11.39	2.1	0.26	0.07	0.52	99.99
Eastern metabasalt	RR-018B	40°30'07.94"	12°13'43.35"	51.33	1.07	13.74	14.04	0.24	7.26	10.41	2.55	0.26	0.08	0.53	101.51
Eastern metabasalt	RR-018C	40°30'08.01"	12°13'43.42"	52.48	1.1	14.19	13.39	0.21	5.68	11.57	1.95	0.18	0.1	0.43	101.28
Eastern metabasalt	RR-018D	40°30'08.08"	12°13'43.48"	51.83	1.06	14.16	13.4	0.21	5.47	13.27	1.39	0.15	0.09	0.48	101.51
Eastern metabasalt	RR-071	40°28'39.28"	11°36'42.51"	54.77	1.46	13.32	15.76	0.26	6.36	10.05	0.65	0.23	0.03	0.85	103.74
Eastern metabasalt	RR-072	40°29'25.44"	11°37'14.46"	54.68	1.52	13.45	15.19	0.22	6.72	9.73	0.41	0.13	0.05	0.67	102.77
Eastern metabasalt	RR-078	40°28'06.14"	11°39'32.83"	52.46	1.15	13.76	13.35	0.21	6.49	10.56	1.68	0.19	0.04	0.63	100.52
Eastern metabasalt	RR-080	40°26'38.53"	11°40'09.08"	51.14	0.97	15.65	13.38	0.2	6.47	10.27	2.88	0.31	0.09	0.6	101.96
Eastern metabasalt	FD-37-001	40°30'22.03"	11°41'07.33"	50.14	0.97	14.33	12.6	0.22	6.47	10.84	1.98	0.09	0.08	0.9	98.62
Eastern metabasalt	FD-37-002	40°30'22.03"	11°41'07.33"	52.47	0.98	14.47	12.95	0.21	6.63	10.72	2.14	0.12	0.07	0.57	101.33
Eastern metabasalt	FD-37-004	40°30'22.03"	11°41'07.33"	51.5	1.11	14.03	14.35	0.23	5.49	9.95	2.08	0.16	0.09	0.36	99.35
Eastern metabasalt	FD-37-005	40°30'22.03"	11°41'07.33"	50.92	1.21	13.21	15.04	0.23	4.97	9.92	2.13	0.15	0.1	0.68	98.56
Eastern metabasalt	FD-37-006	40°30'22.03"	11°41'07.33"	50.81	0.71	15.59	11.17	0.18	7.74	11.18	2.22	0.15	0.06	0.89	100.70
Eastern metabasalt	FD-37-007	40°30'22.03"	11°41'07.33"	51.08	0.99	14.56	13.92	0.21	6.58	9.96	2.57	0.25	0.09	0.92	101.13
Eastern metabasalt	FD-37-009	40°30'22.03"	11°41'07.33"	52.74	0.93	14.95	13.57	0.21	7.53	10.68	2.38	0.18	0.08	0.61	103.86
Eastern metabasalt	FD-37-011	40°30'22.03"	11°41'07.33"	52.94	1.02	13.62	13.86	0.21	6.88	10.32	2.06	0.24	0.04	0.89	102.08
Eastern metabasalt	FD-37-012	40°30'22.03"	11°41'07.33"	53.63	1.23	14.07	15.43	0.25	5.07	10.01	2.36	0.16	0.12	0.88	103.21
Eastern metabasalt	FD-37-013	40°30'22.03"	11°41'07.33"	52.66	0.99	14.75	13.09	0.22	6.23	10.62	2.16	0.18	0.09	0.82	101.81
Eastern metabasalt	FD-37-015	40°30'22.03"	11°41'07.33"	48.91	1.12	15.58	14.27	0.24	6.58	11.58	2.33	0.21	0.1	0.93	101.85
Eastern metabasalt	FD-37-016	40°30'22.03"	11°41'07.33"	48.7	1.28	17.47	13.65	0.18	7.7	9.23	2.04	0.93	0.17	2.46	103.81
Eastern metabasalt	FD-37-019	40°30'22.03"	11°41'07.33"	53.15	0.99	14.19	13.06	0.22	6.16	10.68	2.39	0.13	0.1	0.77	101.84
Eastern metabasalt	FD-016	40°29'24.00"	11°42'01.07"	53.15	1.02	12.62	12.62	0.26	5.85	8.6	2.1	0.34	0.06	0.94	97.56
Eastern metabasalt	FD-028	40°26'43.09"	11°48'24.59"	52.18	1.27	13.24	12.86	0.21	5.74	12.44	1.58	0.24	0.07	0.78	100.61
Western metabasalt	RR-022	40°36'07.38"	12°18'51.47"	49.47	0.95	14.28	12.39	0.23	5.88	10.75	2.3	0.61	0.07	0.76	97.69
Western metabasalt	RR-F1-001	40°29'40.00"	11°53'22.35"	55.52	0.99	14.69	12.23	0.23	7.17	9.34	1.89	0.53	0.1	1.28	103.97
Western metabasalt	RR-F4-006	40°29'31.17"	11°54'14.89"	49.75	1.26	15.1	12.96	0.2	4.74	8.19	3.72	0.31	0.17	0.24	96.64
Western metabasalt	RR-F4-007	40°29'31.17"	11°54'14.89"	49.8	1.35	15.05	12.58	0.19	4.74	7.63	2.33	1.57	0.19	0.32	95.75
Western metabasalt	RR-F6-001	40°29'35.54"	11°53'35.26"	57.06	1.34	16.4	7.24	0.11	2.37	5.92	4.71	1.18	0.2	0.8	97.33
Western metabasalt	RR-F6-002	40°29'35.54"	11°53'35.26"	48.04	1.56	17.37	11.27	0.19	4.64	7.21	4.03	0.99	0.17	0.64	96.11
Western metabasalt	RR-F6-003	40°29'35.54"	11°53'35.26"	46.4	1.45	15.54	12.8	0.24	5.95	8.21	2.93	0.98	0.17	0.68	95.35
Western metabasalt	RR-F6-004	40°29'35.54"	11°53'35.26"	48.72	1.3	14.51	11.68	0.2	5.15	9.4	2.04	0.83	0.19	1.04	95.06
Western metabasalt	RR-F6-005	40°29'35.54"	11°53'35.26"	50.26	1.28	15.5	13.09	0.2	4.94	8.52	3.14	0.96	0.17	0.35	98.41
Western metabasalt	RR-F6-006	40°29'35.54"	11°53'35.26"	50.5	1.34	15.71	12.96	0.2	4.44	8.48	3.53	0.83	0.19	0.26	98.44
Western metabasalt	RR-F6-007	40°29'35.54"	11°53'35.26"	52.73	1.4	15.78	10.57	0.17	4.16	8.13	3.74	0.18	0.2	0.25	97.31
Western metabasalt	RR-F6-008	40°29'35.54"	11°53'35.26"	48.98	1.29	15.2	12.44	0.2	5.18	8.36	3.3	0.91	0.16	0.35	96.37
Western metabasalt	RR-F6-009	40°29'35.54"	11°53'35.26"	48.1	1.33	15.23	13.02	0.22	6.3	8.15	2.59	0.22	0.16	0.14	95.46
Western metabasalt	RR-F6-010	40°29'35.54"	11°53'35.26"	50.64	1.4	15.08	12.75	0.22	5.37	7.19	2.54	0.63	0.18	0.05	96.05
Western metabasalt	RR-F6-016	40°29'35.54"	11°53'35.26"	54.48	0.71	16.43	11.03	0.23	6.07	3.52	4.04	1.19	0.07	2.47	100.24
Western metabasalt	RR-F6-018	40°29'35.54"	11°53'35.26"	53.79	0.63	15.71	9.44	0.2	6.19	9.82	2.35	0.24	0.09	0.77	99.23
Western metabasalt	RR-F16-027	40°29'27.40"	11°53'33.16"	57.24	0.73	14.2	10.32	0.16	5.01	8.5	2.57	0.74	0.05	1.36	100.88
Metadacite	FD-052	40°29'26.72"	11°42'09.52"	70.98	0.34	14.22	5.08	0.07	2.09	1.24	2.02	2.46	0.04	1.55	100.09
Metarhyolite	RR-FST-002	40°29'33.55"	11°42'52.06"	73.2	0.41	11.49	6.58	0.08	1.63	1.81	1.41	2.69	0.08	0.74	100.12

*The coordinates of the samples were obtained based on SIRGAS 2000 Datum.

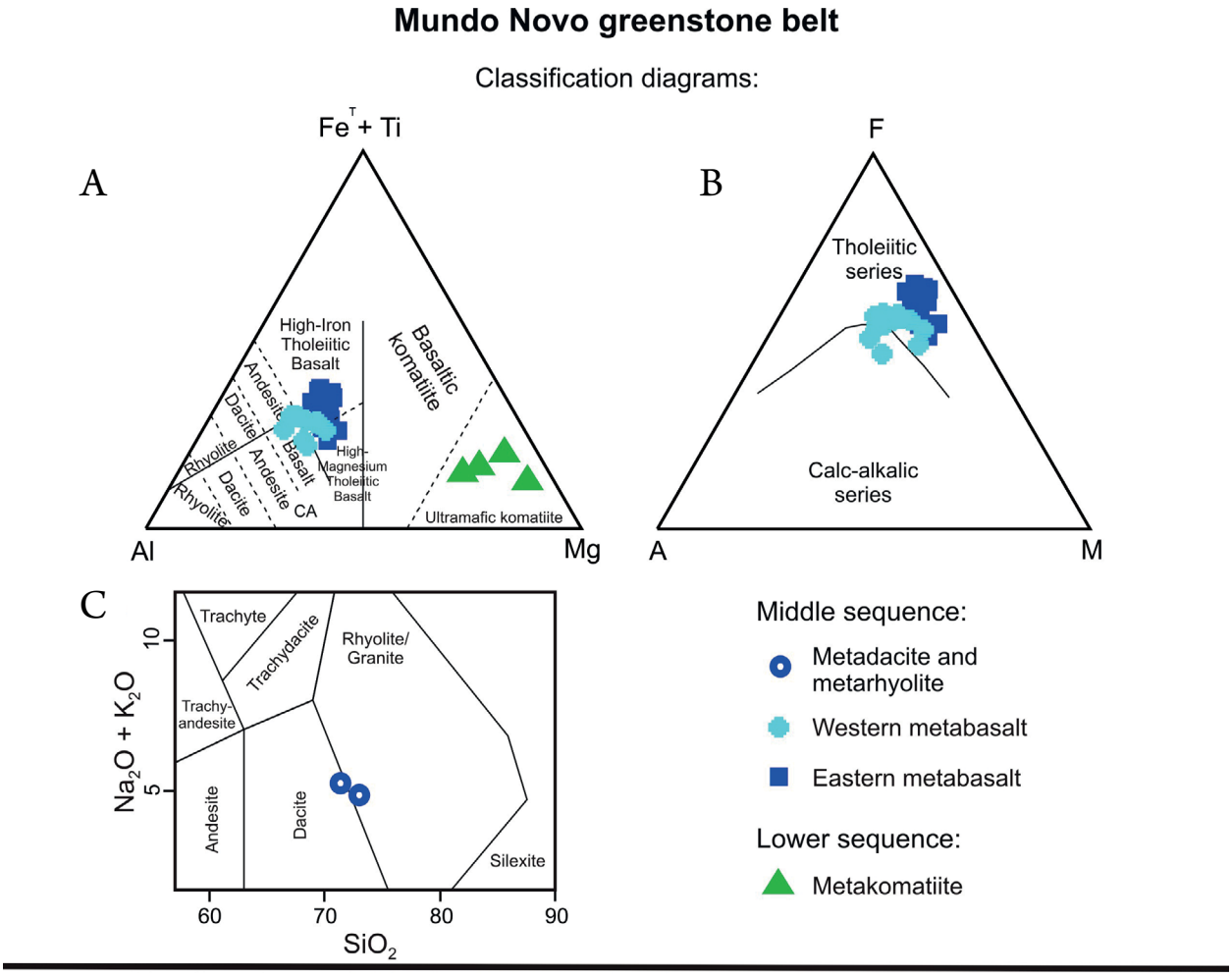

Figure 8. Geochemical diagrams for MNGB rocks. (A) Classification diagram of Jensen (1976): $Fe^T + Ti = FeO + Fe_2O_3 + TiO_2$; $Al = Al_2O_3$; $Mg = MgO$. (B) AFM diagram, tholeiitic and calc-alkalic series (Irvine and Baragar 1971), $A = Na_2O + K_2O$; $F = FeO + 0.8998Fe_2O_3$; $M = MgO$. (C) SiO_2 vs. $Na_2O + K_2O$ classification diagram (Middlemost 1994). Chondrite-normalized REE diagram (Boynton 1984): (D) Metakomatiite in the MNGB lower sequence compared to the metakomatiite in the Barberton greenstone belt (Jahn *et al.* 1982); (E) eastern metabasalt in the MNGB middle sequence; (F) western metabasalt in the MNGB middle sequence; (G) metadacite and metarhyolite in the MNGB middle sequence.

Table 6. Whole-rock REE chemical data (ppm).

Unit and classification	Sample ID	La	Ce	Pr	Nd	Sm	Eu	Gd	Tb	Dy	Ho	Er	Tm	Yb	Lu	ΣREE
Mundo Novo greenstone belt																
Metakomatiite	RR-011B	9.5	13.2	1.18	3.8	0.6	0.2	0.68	0.12	0.74	0.16	0.49	0.07	0.5	0.07	31.1
Metakomatiite	FD-37-017	7.2	12.6	1.62	6.7	1.4	0.43	1.56	0.21	1.49	0.3	0.94	0.13	0.9	0.13	35.61
Metakomatiite	FD-058A	7.1	6.5	1.3	5.3	1.2	0.42	1.6	0.26	1.6	0.32	1	0.14	0.8	0.025	27.56
Metakomatiite	FD-070	4.9	3.7	1.17	4.7	1.3	0.51	1.74	0.29	1.81	0.41	1.11	0.19	1.1	0.11	23.04
Eastern metabasalt	RR-006	5	10.2	1.46	7	2.1	0.76	2.71	0.46	3.01	0.63	1.88	0.26	1.7	0.26	37.43
Eastern metabasalt	RR-011C	10.7	24.1	3.15	14.4	3.7	1.04	4.02	0.64	3.92	0.79	2.25	0.3	1.8	0.27	71.08
Eastern metabasalt	RR-014B	6.4	11.9	1.95	9.3	2.9	1	3.8	0.69	4.83	1.03	3.09	0.45	2.9	0.44	50.68
Eastern metabasalt	RR-018A	7	16.3	2.22	10.3	2.9	1	3.73	0.66	4.31	0.93	2.72	0.41	2.6	0.39	55.47
Eastern metabasalt	RR-018B	7.3	13.4	1.87	9.1	2.8	0.9	3.54	0.61	4.17	0.89	2.69	0.38	2.5	0.38	50.53
Eastern metabasalt	RR-018C	9.3	20.9	2.66	12.1	3.2	1.04	3.9	0.68	4.42	0.96	2.88	0.41	2.7	0.41	65.56
Eastern metabasalt	RR-018D	8	18	2.31	10.7	2.8	0.98	3.58	0.63	4.16	0.91	2.67	0.38	2.5	0.39	58.01
Eastern metabasalt	RR-071	11.6	19.1	2.9	13.1	3.4	1.06	4.63	0.69	4.52	0.87	2.54	0.33	2.1	0.32	67.16
Eastern metabasalt	RR-072	11	24.6	2.93	13.9	3.8	1.28	4.67	0.77	4.6	0.94	2.6	0.37	2.2	0.37	74.03
Eastern metabasalt	RR-078	10	12.8	2.19	10.3	3.1	1.17	4.41	0.75	5.28	1.09	3.39	0.5	3.3	0.51	58.79
Eastern metabasalt	RR-080	10.1	14.1	1.96	8.9	2.7	0.99	3.95	0.71	4.69	0.99	3.09	0.43	2.8	0.46	55.87
Eastern metabasalt	FD-37-001	6.1	12.6	1.83	8.9	2.5	0.99	3.62	0.64	4.28	0.88	2.76	0.38	2.6	0.4	48.48
Eastern metabasalt	FD-37-002	5	11.3	1.7	8.4	2.5	0.96	3.44	0.63	4.21	0.9	2.63	0.37	2.5	0.39	44.93
Eastern metabasalt	FD-37-004	5.7	13.7	2.08	9.9	3.4	1.22	4.39	0.79	5.28	1.15	3.22	0.5	3.3	0.49	55.12
Eastern metabasalt	FD-37-005	6.5	14.9	2.26	10.5	3.2	1.12	4.55	0.78	5.16	1.13	3.4	0.49	3.1	0.49	57.58
Eastern metabasalt	FD-37-006	4.9	8.4	1.2	6.2	1.9	0.7	2.73	0.49	3.09	0.68	1.96	0.3	1.9	0.28	34.73
Eastern metabasalt	FD-37-007	6.2	12	1.77	8.3	2.6	0.94	3.41	0.6	4.31	0.88	2.45	0.4	2.6	0.38	46.84
Eastern metabasalt	FD-37-009	5.7	11.7	1.61	7.9	2.4	0.86	3.31	0.59	4.05	0.83	2.54	0.38	2.4	0.37	44.64
Eastern metabasalt	FD-37-011	6.1	12.7	1.82	8.4	2.5	0.96	3.46	0.6	3.96	0.87	2.63	0.37	2.5	0.41	47.28
Eastern metabasalt	FD-37-012	6.3	14.1	2.02	10	3.3	1.16	4.49	0.77	5.42	1.11	3.33	0.49	3.3	0.48	56.27
Eastern metabasalt	FD-37-013	4.6	11.2	1.7	8.9	2.7	0.97	4	0.71	4.35	0.96	2.86	0.47	2.7	0.43	46.55
Eastern metabasalt	FD-37-015	6.9	12.9	1.91	9.2	3	1.07	4.21	0.73	4.82	1.06	3.12	0.46	3	0.5	52.88
Eastern metabasalt	FD-37-016	6.9	14.8	2.32	11.1	3.7	1.27	4.86	0.87	5.5	1.22	3.64	0.52	3.4	0.54	60.64
Eastern metabasalt	FD-37-019	7.1	14.1	1.95	9.3	2.8	1	3.62	0.67	4.45	0.96	2.81	0.42	2.8	0.46	52.44
Eastern metabasalt	FD-016	7.4	12	1.94	9	2.6	0.94	3.78	0.65	4.42	0.92	2.93	0.39	2.6	0.4	49.97
Eastern metabasalt	FD-028	5.7	13.1	1.99	10.2	3.2	1.12	4.34	0.72	4.82	1	2.92	0.44	2.9	0.42	52.87
Western metabasalt	RR-022	18.6	27.6	4.74	19.2	4.8	1.42	4.98	0.84	5.49	1.14	3.28	0.48	3.1	0.44	96.11
Western metabasalt	RR-F1-001	21.1	39.1	5.18	20	4.7	1.41	5.23	0.84	5.07	0.98	2.72	0.38	2.6	0.41	109.72
Western metabasalt	RR-F4-006	23	44.3	5.6	23.4	5.5	1.54	6.15	1	6.56	1.33	4	0.57	3.8	0.56	127.31
Western metabasalt	RR-F4-007	25	45.8	5.79	23.4	5.6	1.59	6.4	1.04	6.79	1.31	3.94	0.56	3.7	0.58	131.5
Western metabasalt	RR-F6-001	25.8	48.7	6.24	24.9	5.7	1.45	6.51	1.06	6.74	1.32	3.79	0.59	3.7	0.55	137.05
Western metabasalt	RR-F6-002	26.5	55.2	7.1	28.2	6.8	1.67	7.62	1.22	7.71	1.56	4.58	0.66	4.4	0.64	153.86
Western metabasalt	RR-F6-003	27.7	47.5	5.96	24.3	5.8	1.63	6.67	1.1	6.86	1.42	4.26	0.67	4	0.66	138.53
Western metabasalt	RR-F6-004	23.9	45.4	5.88	23.6	5.9	1.4	6.56	1.08	6.87	1.41	3.99	0.6	3.8	0.54	130.93
Western metabasalt	RR-F6-005	23.4	45.9	5.91	24.2	5.8	1.72	6.58	1.06	6.59	1.38	4.26	0.58	3.9	0.6	131.88
Western metabasalt	RR-F6-006	21.7	45.1	5.82	23	5.7	2.06	6.48	1	6.67	1.37	4.12	0.56	3.8	0.58	127.96
Western metabasalt	RR-F6-007	22.2	45.8	6.05	24.2	5.8	2.01	6.86	1.09	6.9	1.39	4.13	0.59	3.9	0.6	131.52
Western metabasalt	RR-F6-008	23.9	48	6.04	24.8	6	1.93	6.65	1.05	6.62	1.32	3.99	0.6	3.8	0.58	135.28
Western metabasalt	RR-F6-009	21.3	44.8	5.84	23.9	5.9	1.82	6.59	1.02	6.79	1.36	4.15	0.57	3.8	0.57	128.41
Western metabasalt	RR-F6-010	23	44.3	5.79	23.6	5.4	1.56	6.8	1.04	6.61	1.36	4	0.66	3.8	0.61	128.53
Western metabasalt	RR-F6-016	10.9	19.2	2.35	9.5	2	0.53	2.59	0.43	3.01	0.72	2.09	0.33	2.2	0.34	56.19
Western metabasalt	RR-F6-018	16.2	31.8	3.92	15.7	3.4	0.98	3.88	0.61	3.66	0.77	2.34	0.34	2.1	0.35	86.05
Western metabasalt	RR-F16-027	24.1	30.9	3.65	14.2	3.1	0.83	3.61	0.56	3.64	0.75	2.17	0.35	2.1	0.33	90.29
Metadacite	FD-052	16.3	29.8	2.97	12.4	2.8	0.69	2.62	0.43	2.81	0.52	1.54	0.18	1.3	0.16	74.52
Metarhyolite	RR-FST-002	35.5	64.4	6.27	23.9	4.4	0.94	4.09	0.6	3.66	0.73	2.25	0.27	2.2	0.26	149.47

Table 7. Whole-rock trace and minor element chemical data (ppm).

Unit and classification	Sample ID	Cs	Ba	Th	U	Ta	Nb	Zr	Hf	Ti	Y	Sr	Rb	Ni	V
Mundo Novo greenstone belt															
Metakomatiite	RR-011B	0.37	5	1.2	0.35	0.025	2.45	13	0.53	1500	4.47	12	1.2	945	2.5
Metakomatiite	FD-37-017	0.51	176	2.8	1.38	0.3	1.69	43	1.31	1380	8.83	49	10.3	644	42
Metakomatiite	FD-058A	0.06	42	2.6	0.72	0.36	1.27	20	0.63	420	10.47	5	1.6	587	2.5
Metakomatiite	FD-070	0.11	50	0.8	0.39	0.025	0.58	15	0.2	420	12.02	5	1	493	2.5
Eastern metabasalt	RR-006	0.76	104	0.5	0.16	0.025	3.3	40	1.27	4980	18.07	90	8.1	115	207
Eastern metabasalt	RR-011C	1.52	134	2.3	0.66	0.17	7.32	93	2.48	7140	21.67	100	8.1	110	232
Eastern metabasalt	RR-014B	0.13	122	0.8	0.13	0.025	2.66	69	1.96	6000	28.43	108	6.1	112	283
Eastern metabasalt	RR-018A	0.3	110	1.8	0.31	0.025	5.3	77	2.15	6240	26.24	109	4	112	295
Eastern metabasalt	RR-018B	0.21	80	1	0.27	0.025	3.59	67	1.87	6420	24.46	120	5.8	110	306
Eastern metabasalt	RR-018C	0.17	132	1.8	0.42	0.025	9.69	75	1.99	6600	27.2	128	2.1	112	306
Eastern metabasalt	RR-018D	0.16	119	2.7	0.42	0.34	7.56	72	2.07	6360	25.88	162	1.8	109	292
Eastern metabasalt	RR-071	0.77	73	2.3	0.31	0.025	5.52	84	2.52	8760	22.27	66	5.2	92	306
Eastern metabasalt	RR-072	0.36	30	1.1	0.29	0.025	4.77	88	2.71	9120	22.77	185	4	97	315
Eastern metabasalt	RR-078	0.25	242	0.8	0.29	0.025	3.08	69	2.23	6900	28.29	94	7.6	125	315
Eastern metabasalt	RR-080	0.27	102	0.9	0.39	0.025	2.91	83	2	5820	24.88	133	11.7	124	386
Eastern metabasalt	FD-37-001	0.2	108	0.4	0.35	0.025	2.26	78	1.97	5820	22.32	109	2.6	90	366
Eastern metabasalt	FD-37-002	0.17	46	0.1	0.22	0.025	1.93	69	1.99	5880	22.86	110	2.8	108	371
Eastern metabasalt	FD-37-004	0.09	40	0.4	0.23	0.025	2.46	85	2.28	6660	27.81	107	2.3	72	423
Eastern metabasalt	FD-37-005	0.07	34	0.4	0.26	0.025	2.75	91	2.36	7260	29.87	127	1.6	62	425
Eastern metabasalt	FD-37-006	0.41	53	0.05	0.18	0.025	1	48	1.37	4260	16.4	107	4.9	152	298
Eastern metabasalt	FD-37-007	0.42	232	0.3	0.24	0.025	1.99	79	1.91	5940	23.31	122	6.6	142	362
Eastern metabasalt	FD-37-009	0.24	185	0.2	0.24	0.025	1.84	73	1.87	5580	22.88	117	3.3	164	374
Eastern metabasalt	FD-37-011	0.29	127	0.5	0.27	0.025	4.03	56	1.69	6120	22.3	111	4.7	148	299
Eastern metabasalt	FD-37-012	0.12	40	0.4	0.27	0.025	3.5	96	2.41	7380	28.27	109	2	49	490
Eastern metabasalt	FD-37-013	0.41	54	0.05	0.21	0.025	2.23	73	1.93	5940	22.35	113	4.6	106	379
Eastern metabasalt	FD-37-015	0.51	116	0.2	0.27	0.025	2.62	87	2.15	6720	26.05	120	5.5	116	415
Eastern metabasalt	FD-37-016	1.29	768	5	0.47	1.61	4.5	96	3.96	7680	28.83	107	32.9	110	451
Eastern metabasalt	FD-37-019	0.09	35	0.7	0.27	0.025	2.52	77	2.16	5940	23.28	112	1.5	77	409
Eastern metabasalt	FD-016	0.32	161	1.5	0.36	0.14	2.64	78	2.09	6120	24.9	111	8.2	104	323
Eastern metabasalt	FD-028	0.92	56	0.7	0.21	0.17	2.92	75	1.91	7620	25.05	132	8.9	111	322
Western metabasalt	RR-022	0.31	78	1.9	0.46	0.32	5.25	87	2.36	5700	28.44	574	13.7	83	192
Western metabasalt	RR-F1-001	1.2	141	4.2	0.95	0.025	6.22	138	3.44	5940	25.4	127	16.3	148	257
Western metabasalt	RR-F4-006	0.12	72	3.4	1.06	0.15	7.06	169	4.5	7560	32.18	187	4.5	88	331
Western metabasalt	RR-F4-007	0.63	480	3.3	1.08	0.08	7.8	171	4.31	8100	35.3	180	46.2	89	338
Western metabasalt	RR-F6-001	1.6	216	4.4	1.39	0.26	9.05	177	4.94	8040	32.77	131	43.7	106	358
Western metabasalt	RR-F6-002	1.9	188	4.3	1.3	0.24	8.7	192	5.27	9360	40.14	108	29.5	91	312
Western metabasalt	RR-F6-003	1.11	244	3.6	1.16	0.025	8.05	183	4.73	8700	36.53	127	19.8	97	366
Western metabasalt	RR-F6-004	1.31	184	3.3	1.09	0.025	7.05	161	4.52	7800	33.53	80	20.9	93	310
Western metabasalt	RR-F6-005	2.57	278	3.3	1.09	0.025	7.1	171	4.45	7680	34.07	205	19.2	92	316
Western metabasalt	RR-F6-006	0.46	228	3.3	1.11	0.025	7.49	167	4.41	8040	36.03	214	16.5	91	322
Western metabasalt	RR-F6-007	0.12	98	3.4	1.11	0.025	7.34	172	4.32	8400	35.58	148	2.7	86	322
Western metabasalt	RR-F6-008	1.01	157	3.2	1.01	0.025	6.82	163	4.46	7740	34.29	152	16.5	88	326
Western metabasalt	RR-F6-009	0.19	55	3.2	1.03	0.025	7.48	162	4.4	7980	37.08	204	3.3	93	319
Western metabasalt	RR-F6-010	0.55	184	3.1	1.08	0.025	7.51	170	4.36	8400	34.44	171	12.2	89	328
Western metabasalt	RR-F6-016	2	130	2.8	0.96	0.025	4.54	130	3.07	4260	17.1	54	27.2	51	241
Western metabasalt	RR-F6-018	0.33	59	2.7	0.93	0.025	4.04	118	2.86	3780	20.71	220	4.3	82	221
Western metabasalt	RR-F16-027	0.55	136	3.1	1.08	0.31	2.85	121	2.82	4380	20.78	112	21.5	80	313
Metadacite	FD-052	3.29	553	7	5.24	1.01	9.57	83	2.72	2040	14.94	109	92.3	99	76
Metarhyolite	RR-FST-002	5.83	631	17.1	5.37	0.26	8.37	152	4.88	2460	19.91	144	95.3	49	67

an average of 1.38 (σ = 0.13) for the western metabasalt and of 1.21 (σ = 0.21) for the eastern one (Tab. 8). Eu/Eu* ratios indicate subtle negative anomalies of europium more accentuated to western metabasalt (average = 0.83 and σ = 0.09; Tab. 8) than the Eu/Eu* ratio values of the eastern metabasalt (average = 0.93 and σ = 0.04; Tab. 8). The Ce/Ce* ratios for the eastern metabasalt have an average of 6.12 (σ = 0.81), different from the western metabasalt, with an average value of 9.15 (σ = 1.43; Tab. 8), in addition to the ΣREE average value for the eastern metabasalt of 53.68 (σ = 9.26), which is significantly lower than the ΣREE average value of 120.06 (σ = 24.47) of the western metabasalt (Tab. 6).

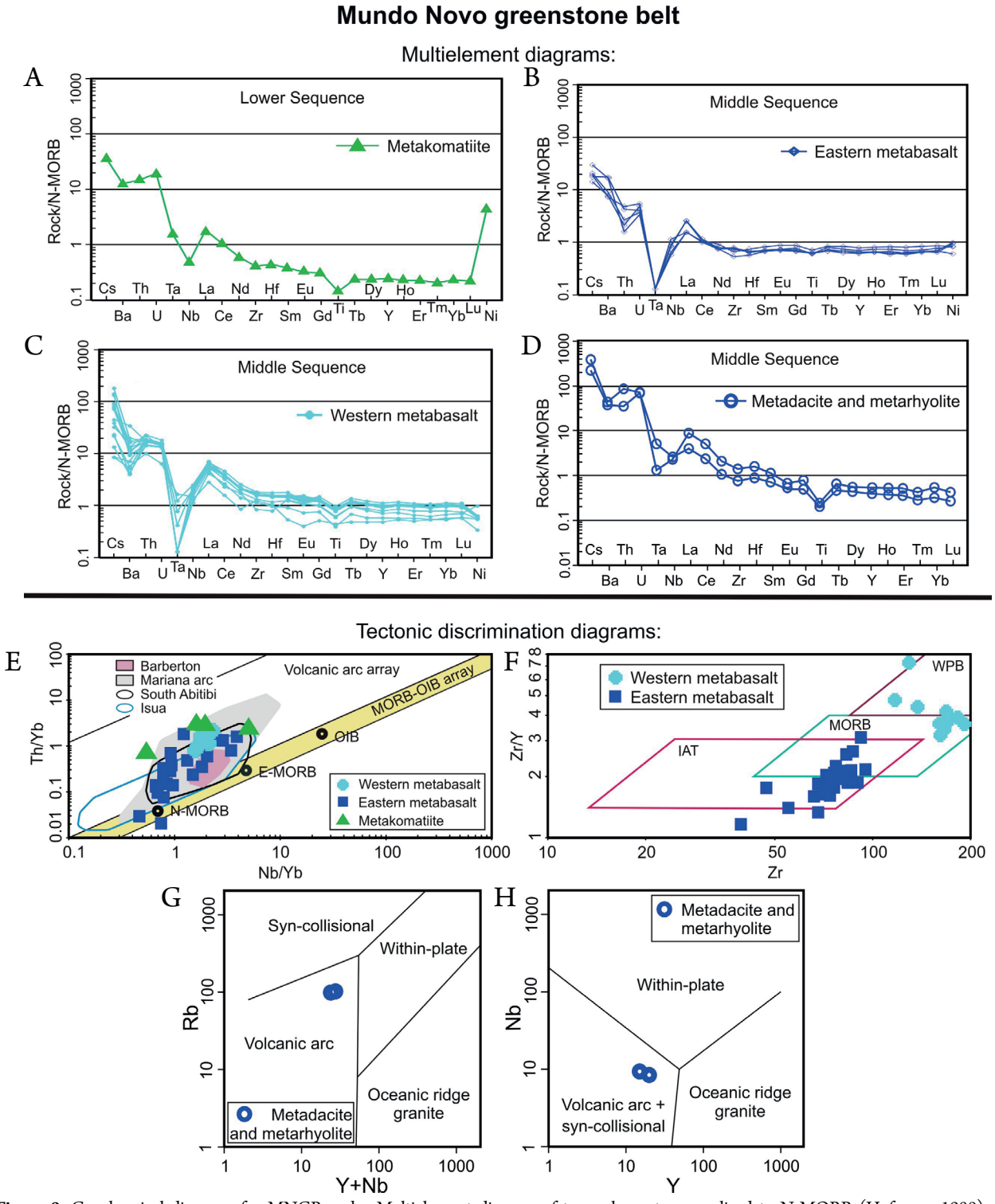

Figure 9. Geochemical diagrams for MNGB rocks. Multielement diagram of trace elements normalized to N-MORB (Hofmann 1988): (A) metakomatiite in the MNGB lower sequence; (B) eastern metabasalt in the MNGB middle sequence; (C) western metabasalt in the middle sequence; (D) metadacite and metarhyolite in the MNGB middle sequence. Tectonic setting discrimination diagram: (E) metakomatiite and eastern and western metabasalts in the MNGB lower and middle sequences plotted in the Nb/Yb-Th/Yb diagram (N-MORB: Normal – Middle ocean ridge basalts, E-MORB: Enriched – Middle ocean ridge basalts, OIB: Ocean island basalts; Pearce 2008) compared with basalts from South Abitibi (Kerrich and Xie 2002, Xie and Kerrich 1994), Barberton (Jochum *et al.* 1991, Parman *et al.* 1997, Chavagnac 2004) and Isua Archean greenstone belts (Polat and Hoffmann 2003, Polat *et al.* 2002) and the Mariana Arc (Pearce *et al.* 2005); (F) eastern and western metabasalts in the MNGB middle sequence plotted in the Zr-Zr/Y diagram (IAT: Island arc tholeiitic, MORB: Middle ocean ridge basalts, WPB: Within-plate basalts); (G and H) metadacite in the MNGB middle sequence plotted in the Y + Nb-Rb and Y-Nb diagrams (Pearce *et al.* 1984).

Table 8. Major, REE and trace element ratios.

Unit and classification	Sample ID	Zr/Y	CaO/Al_2O_3	$(La/Yb)_N$	$(Gd/Yb)_N$	Eu/Eu*	Ce/Ce*
Mundo Novo greenstone belt							
Metakomatiite	RR-011B	-	0.41	12.80	1.09	0.96	3.96
Metakomatiite	FD-37-017	-	1.42	5.39	1.39	0.89	5.12
Metakomatiite	FD-058A	-	1.10	5.98	1.61	0.93	3.13
Metakomatiite	FD-070	-	2.63	3.00	1.27	1.04	2.68
Average		-	1.39	6.79	1.34	0.95	3.72
Standard deviation (σ)		-	0.92	4.21	0.21	0.06	1.07
Eastern metabasalt	RR-006	2.21	-	1.98	1.29	0.97	5.54
Eastern metabasalt	RR-011C	4.29	-	4.01	1.80	0.82	7.65
Eastern metabasalt	RR-014B	2.43	-	1.49	1.06	0.92	5.67
Eastern metabasalt	RR-018A	2.93	-	1.82	1.16	0.93	6.88
Eastern metabasalt	RR-018B	2.74	-	1.97	1.14	0.87	5.54
Eastern metabasalt	RR-018C	2.76	-	2.32	1.17	0.90	7.15
Eastern metabasalt	RR-018D	2.78	-	2.16	1.16	0.95	6.81
Eastern metabasalt	RR-071	3.77	-	3.72	1.78	0.82	6.19
Eastern metabasalt	RR-072	3.86	-	3.37	1.71	0.93	7.40
Eastern metabasalt	RR-078	2.44	-	2.04	1.08	0.97	4.75
Eastern metabasalt	RR-080	3.34	-	2.43	1.14	0.93	4.75
Eastern metabasalt	FD-37-001	3.49	-	1.58	1.12	1.01	5.96
Eastern metabasalt	FD-37-002	3.02	-	1.35	1.11	1.00	6.22
Eastern metabasalt	FD-37-004	3.06	-	1.16	1.07	0.97	6.89
Eastern metabasalt	FD-37-005	3.05	-	1.41	1.18	0.90	6.84
Eastern metabasalt	FD-37-006	2.93	-	1.74	1.16	0.94	4.63
Eastern metabasalt	FD-37-007	3.39	-	1.61	1.06	0.97	5.64
Eastern metabasalt	FD-37-009	3.19	-	1.60	1.11	0.93	5.72
Eastern metabasalt	FD-37-011	2.51	-	1.65	1.12	1.00	5.98
Eastern metabasalt	FD-37-012	3.40	-	1.29	1.10	0.92	6.50
Eastern metabasalt	FD-37-013	3.27	-	1.15	1.20	0.90	6.57
Eastern metabasalt	FD-37-015	3.34	-	1.55	1.13	0.92	5.65
Eastern metabasalt	FD-37-016	3.33	-	1.37	1.15	0.92	6.61
Eastern metabasalt	FD-37-019	3.31	-	1.71	1.04	0.96	5.92
Eastern metabasalt	FD-016	3.13	-	1.92	1.17	0.92	5.18
Eastern metabasalt	FD-028	2.99	-	1.33	1.21	0.92	6.59
Average		3.11	-	1.91	1.21	0.93	6.12
Standard deviation (σ)		0.46	-	0.74	0.21	0.04	0.81
Western metabasalt	RR-022	3.06	-	4.05	1.30	0.89	7.71
Western metabasalt	RR-F1-001	5.43	-	5.47	1.62	0.87	8.89
Western metabasalt	RR-F4-006	5.25	-	4.08	1.31	0.81	9.45
Western metabasalt	RR-F4-007	4.84	-	4.56	1.40	0.81	9.45
Western metabasalt	RR-F6-001	5.40	-	4.70	1.42	0.73	10.02
Western metabasalt	RR-F6-002	4.78	-	4.06	1.40	0.71	11.27
Western metabasalt	RR-F6-003	5.01	-	4.67	1.35	0.80	9.39
Western metabasalt	RR-F6-004	4.80	-	4.24	1.39	0.69	9.68
Western metabasalt	RR-F6-005	5.02	-	4.05	1.36	0.85	9.83
Western metabasalt	RR-F6-006	4.64	-	3.85	1.38	1.04	9.98
Western metabasalt	RR-F6-007	4.83	-	3.84	1.42	0.97	10.18
Western metabasalt	RR-F6-008	4.75	-	4.24	1.41	0.93	10.06
Western metabasalt	RR-F6-009	4.37	-	3.78	1.40	0.89	10.05
Western metabasalt	RR-F6-010	4.94	-	4.08	1.44	0.79	9.64
Western metabasalt	RR-F6-016	7.60	-	3.34	0.95	0.71	5.87
Western metabasalt	RR-F6-018	5.70	-	5.20	1.49	0.82	7.85
Western metabasalt	RR-F16-027	5.82	-	7.74	1.39	0.76	6.21
Average		5.07	-	4.47	1.38	0.83	9.15
Standard deviation (σ)		0.89	-	0.99	0.13	0.09	1.43
Metadacite	FD-052	-	-	8.45	1.62	0.77	6.63
Metarhyolite	RR-FST-002	-	-	10.87	1.50	0.67	9.90
Average		-	-	9.66	1.56	0.72	8.86
Standard deviation (σ)		-	-	1.71	0.09	0.07	2.31

The geochemical data of the major and trace elements normalized to the fertile mantle MORB (FMM) values as a tectonic setting marker (Pearce and Parkinson 1993) are similar for both metabasalt types of the MNGB. The patterns in which normalized Nb (24.06) and Zr (11.48) > TiO_2 (6.47) and in which Y (6.98) and Yb (7.04) ≥ CaO (3.00), Al_2O_3 (3.91) and V (4.20) into the two metabasalts are similar to the patterns in ocean floor basalts in a back-arc basin system, as demonstrated in the Barberton greenstone belt (Furnes *et al.* 2013).

In the multielement diagram of trace elements normalized to N-MORB (Hofmann 1988; Figs. 9B and 9C), both metabasalt groups show enrichments of Cs, Ba, Th, U and LREE relative to Ta, Nb, Zr, Hf, Ti, Y and heavy rare earth elements (HREE), a flat pattern from Lu to Zr, and a negative Ta anomaly. The difference between the two groups is subtle but consistent, as for example, the negative Ti anomaly is more accentuated in the western metabasalt than in the eastern one, the western metabasalt is more enriched in La, Ce, and Nd than the eastern, and the Th, U, and Cs values of the western metabasalt are greater than the values of the same elements in the eastern metabasalt.

The Nb/Yb-Th/Yb discrimination diagram of immobile elements in the eastern and western metabasalts of the MNGB indicates a trend that extends from N-MORB in the MORB-Ocean island basalts (OIB) array to the volcanic arc array, with a principal axis of dispersion of the plots oblique to the MORB-OIB array (Fig. 9E). This pattern is similar to oceanic subduction-related basalts of the Mariana Arc and Isua, Barberton and South Abitibi Archean greenstone belts (Fig. 9E). The eastern metabasalt has an IAT-type pattern, with some samples overlapping the MORB field, and the western metabasalt mainly features a MORB pattern with a few occurrences plotting in the within-plate basalt field (WPB; Fig. 9F). Thus, the Zr/Y ratio values for the eastern metabasalt with an average of 3.11 ($\sigma = 0.46$) are lower than the values of the western metabasalt, that show an average of 5.07 ($\sigma = 0.89$; Tab. 8).

Metadacite and subordinate metarhyolite

The felsic metavolcanic rocks of the middle sequence of the MNGB are classified as metadacite and subordinate metarhyolite in the SiO_2 *vs.* $Na_2O + K_2O$ diagram (Middlemost 1994; Fig. 8C). The chondrite-normalized REE diagram (Boynton 1984) for these felsic metavolcanic rocks subtly slopes from Lu to Gd, as shown by $(Gd/Yb)_N$ ratios average of 1.56 ($\sigma = 0.09$; Tab. 8), with a negative Eu anomaly (Fig. 8G), as indicated by the average Eu/Eu* ratio of 0.72 ($\sigma = 0.07$; Tab. 8). There is enrichment in LREE with strong fractionation from Sm to La also shown by the average of the $(La/Yb)_N$ ratio of 9.66 ($\sigma = 1.71$; Tab. 8). The average of the Ce/Ce* ratio is 8.86 ($\sigma = 2.31$; Tab. 8) and the ΣREE value for the metadacite sample is 74.52 and for the metarhyolite sample the ΣREE value obtained was 149.47 (Tab. 6).

In the N-MORB-normalized multielement diagram (Hofmann 1988; Tab. 7; Fig. 9D), the metadacite is enriched in Nb and Ta; high Cs, Ba, Th and U values, a negative Ti anomaly and moderate values of Hf (2.72–4.88 ppm) and Zr (83–152 ppm) are shown. Moreover, the metadacite and subordinate metarhyolite plot in the volcanic arc field in the tectonic diagrams of Pearce *et al.* (1984; Figs. 9G and 9H).

DISCUSSION

The fine-grained microstructure of the metakomatiite in the MNGB is composed of skeletal grains with planar growths that intersect each other and do not intercept former structures, which indicates a relict spinifex microstructure preserved in chilled margins of the komatiite flows. This spinifex microstructure in the metakomatiite and the occurrence of pillow lava structure in the eastern metabasalt suggest rapid and subaquatic crystallization such as that widely observed and interpreted in other greenstone belt terrains (Anhaeusser 2014). The lithological association of the volcanic rocks of the MNGB with the metachert and BIF, the absence of zircon xenocrysts, the manganiferous ilmenite occurrence in the western metabasalt and the carbonate and argilic-chloritic hydrothermal alteration zones developed on the western metabasalt indicate ocean floor settings (Zucchetti *et al.* 2000a, 2000b, Grachev *et al.* 2011, Spreafico 2017).

The effect of the fractional crystallization and heterogeneous intraoceanic crustal contamination during the rise of the magma in the eastern and western metabasalts of the MNGB may explain the differences in the mineral paragenesis. The eastern metabasalt, for example, is composed mainly of anorthite, bytownite, magnesiohornblende, ferrohornblende, augite, edenite, and quartz; the western metabasalt comprises oligoclase, andesine, actinolite, ferrotschermakite, magnesiohornblende, biotite, and quartz.

Enrichments of Cs, Ba, Th, and LREE relative to Ta, Nb, Zr, Hf, Ti, Y and HREE and the flat pattern from Lu to Nd in the multielement diagram (Figs. 9A, 9B and 9C) show that the metakomatiite and the two metabasalts of the MNGB were generated from the metasomatized mantle above the subducting altered oceanic crust; Furnes *et al.* (2013) interpreted a similar enrichment in the Onverwacht Suite in the Barberton greenstone belt. However, the enrichment of LREE relative to HREE in the chondrite-normalized REE diagram (Boynton 1984; Figs. 8E and 8F) was more accentuated in the metakomatiite, which shows average values of the $(La/Yb)_N$ and $(Gd/Yb)_N$ ratios of 6.79 and 1.34, respectively, and in the tholeiitic-calc-alkalic western metabasalt, which shows higher average values of the $(La/Yb)_N$ and $(Gd/Yb)_N$ ratios of 4.47 and 1.38, respectively, relative to the high-iron tholeiitic eastern metabasalt, which shows average values of 1.91 and 1.21, respectively. In this sense, the ΣREE average value to the western metabasalt of 120.06 is also significantly greater than the ΣREE average value to the eastern metabasalt of 53.68 and the ΣREE average value to the metakomatiite of 29.32.

High Ce/Ce* ratio values to metadacite (6.63) and metarhyolite (9.90) may be explained by the trace concentration of zircon in these rocks. Thus, it opens the possibility of the occurrence of zircon in the western metabasalt, which also has high Ce/Ce* ratio average values of 9.15.

Eu/Eu* ratio values form a downward trend from the eastern metabasalt (average of 0.93) to metadacite (value of 0.77)

with the western metabasalt (average of 0.83) showing intermediate values. The greater concentration of plagioclase, with emphasis on calcic plagioclase, in the eastern metabasalt than the western metabasalt and metadacite may explain the Eu/Eu* ratio relation among them. In this case, we consider the fractional crystallization of plagioclase with the early crystallization of the calcic plagioclase in the eastern metabasalt, the main crystallization of sodic plagioclase in the western metabasalt and the low plagioclase content in the metadacite.

Both the eastern and western metabasalt samples of the MNGB plot in the IAT, MORB and WPB fields in the Zr-Zr/Y diagram (Fig. 9F); the eastern metabasalt plots in the IAT and MORB fields, due to low values of Zr and Zr/Y ratio, and the western metabasalt, which has higher values of the same element and ratio, plots in the MORB and WPB field. The duplicity of fields by each metabasalt type in the Zr-Zr/Y diagram appears initially uncertain; however, the proximity of settings during volcanism and the transition from one setting to the other due to tectonic events must be considered. Therefore, it is possible that the eastern and western metabasalts are cogenetic and consistent with nearby intraoceanic settings in the MNGB, such as an island arc, which is more consistent with the eastern metabasalt data, and a back-arc basin, which is more coherent with the western metabasalt data, although with different levels of intraoceanic crustal contamination during the formation, as for example, by subduction components.

The plots of the metakomatiite and eastern and western metabasalts of the MNGB in the Nb/Yb-Th/Yb diagram feature a steep vector oblique to the MORB-OIB array (Fig. 9E). Those MNGB plots extend from near the N-MORB point, in the MORB-OIB array, and enter the field of the volcanic arc array, avoiding the OIB point. This plot distribution is similar to the South Abitibi (Kerrich and Xie 2002, Xie and Kerrich 1994), Barberton (Jochum *et al.* 1991, Parman *et al.* 1997, Chavagnac 2004), and Isua (Polat and Hoffmann 2003, Polat *et al.* 2002) Archean greenstone belts (Fig. 9E), which are interpreted as an intraoceanic provenance as discussed in Pearce (2008), and similar to the modern Mariana intraoceanic arc-basin system (Pearce *et al.* 2005). Moreover, the MNGB geochemical pattern observed in the Nb/Yb-Th/Yb diagram shows that a subduction-related setting, in this case an intraoceanic arc, contributes to the increase in Th content in the rocks displacing the samples from the MORB-OIB array to the volcanic arc array. Therefore, the eastern metabasalt samples remaining in the MORB-OIB array register the initial ocean crust in the MNGB and, with increasing island arc input, the plots displace from the MORB-OIB array. However, the western metabasalt, which could initially be formed in a back-arc basin, was affected by intraoceanic crustal contamination, probably because of the subduction components of the island arc during the rise of the magma, which totally displaced the samples from the MORB-OIB array.

The metadacite samples of the MNGB plot in the volcanic arc field in the diagrams of Pearce *et al.* (1984; Figs. 9G and 9H), thus excluding intracratonic possibilities. In addition, the $(La/Yb)_N$ ratio of 8.45 in the metadacite may be interpreted as an oceanic crust setting with a slight crustal input subducting the oceanic crust according to Condie and Kronër (2013).

Rios (2017) interpreted an intraoceanic setting with a back-arc provenance for basalts in the Neoarchean Contendas-Mirante volcano-sedimentary sequence, which is also inserted in the Contendas-Jacobina Lineament (southern part); this volcano-sedimentary sequence is similar and coeval relative to the MNGB. In the Archean Rio das Velhas greenstone belt, southern São Francisco Craton, ocean floor metabasalts and the felsic volcanic rocks were interpreted as occurrences of island arc or back-arc basin settings (Zucchetti *et al.* 2000a, 2000b), which we also interpreted in the MNGB.

Differently, an intracontinental provenance has been described for the Umburanas greenstone belt, in the southern part of the Gavião Block in the eastern São Francisco Craton (Leal *et al.* 2003), with deposition over a continental crust. This provenance suggests a diversity of settings for the greenstone belts in the São Francisco Craton, more specifically in the Gavião Block.

Therefore, the intraoceanic arc-basin system appears suitable for defining the tectonic setting of the MNGB, such as other greenstone and volcano-sedimentary sequences in the São Francisco Craton. In addition, the volcanic rocks would have formed in back-arc basin and island arc settings at 2595 ± 21 Ma, considering the hypothesis that these rocks of the lower and middle sequences sourced from the same magma. Thus, the oceanic crust in which the MNGB was formed was amalgamated between cratonic blocks (Gavião, Mairi, Jequié and Serrinha blocks and Itabuna-Salvador-Curaçá Belt) of the northern and eastern São Francisco Craton in the Orosirian period (Leite 2002; Figs. 10A and 10B), forming the north-south trend Contendas-Jacobina Lineament within which the greenstone lies.

CONCLUSIONS

The mineralogical and geochemical particularities between the eastern and western metabasalts are products of the intraoceanic crustal contamination during the rise of the magma, fractional crystallization and the formation in nearby but different settings such as the back-arc basin and island arc tholeiitic. Thus, we strongly consider the possibility that the volcanic rocks of the MNGB have sourced from the same magma.

The volcanic rocks in the MNGB were formed in an intraoceanic arc-basin system at 2595 ± 21 Ma. The eastern and western metabasalts were formed in the near back-arc basin and island arc settings, with an IAT pattern for the eastern metabasalt and a MORB pattern for the western metabasalt, suggesting the back-arc basin setting to the latter. The intraoceanic crustal input in the oceanic arc system enriched the Cs, Ba, Th, and LREE content in the metakomatiite, eastern and western metabasalts, and the metadacite of the MNGB, with most accentuated values in the western metabasalt and metadacite suggesting that these rocks were the most affected by intraoceanic contamination during the volcanic processes.

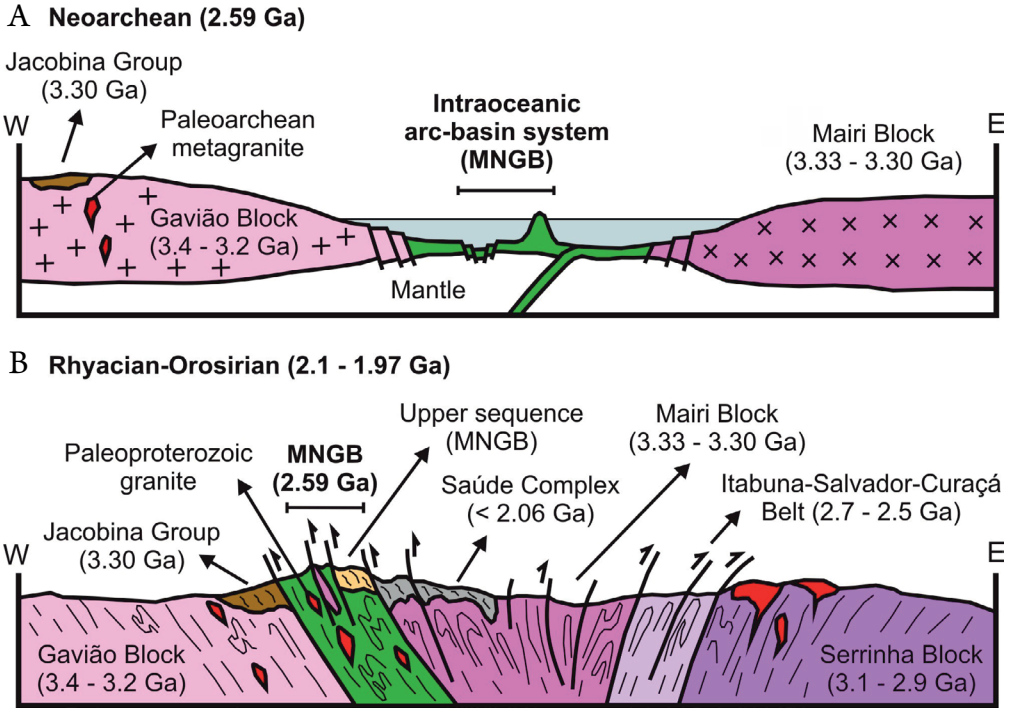

Figure 10. Intraoceanic setting proposed for the MNGB formation based on new data presented in this study and compiled ages for the Gavião Block, MNGB and Rhyacian-Orosirian granites (Mougeot 1996, Leite 2002, Peucat *et al.* 2002, Zincone *et al.* 2016, Spreafico 2017, Spreafico *et al.* 2018), Mairi Block (Sousa *et al.* 2018), Jacobina Group (Teles 2013, Teles *et al.* 2015, Barbuena *et al.* 2016), Serrinha Block (Oliveira *et al.* 2002a, 2002b, Rios *et al.* 2009), Itabuna-Salvador-Curaçá Belt (Silva *et al.* 1997, Oliveira *et al.* 2010), and Saúde Complex (Barbuena *et al.* 2016, Zincone *et al.* 2017). (A) Island arc tholeiitic and back-arc basin between the Gavião and Mairi blocks and formation of the MNGB at 2595 Ma. (B) Rhyacian-Orosirian tectonic event that compressed the MNGB between the cratonic blocks of the eastern São Francisco Craton.

The intraoceanic provenance of the MNGB is comparable to the Contendas-Mirante volcano-sedimentary sequence. Furthermore, both of which are placed in the Contendas-Jacobina Lineament and have geological and tectonic similarities relative to other greenstones in other parts of the São Francisco Craton, such as the Rio das Velhas greenstone belt.

The MNGB rocks were compressed between cratonic blocks of the eastern São Francisco Craton during the Rhyacian-Orosirian period, thus forming the Contendas-Jacobina Lineament within which the greenstone lies.

In order to improve the interpretations present in this manuscript, additional geochronology and Lu-Hf isotope studies could contribute to a more thorough understanding of the geology and tectonic history of the MNGB.

ACKNOWLEDGMENTS

This research was linked to the PhD program of the *Instituto de Geociências, Universidade Federal da Bahia*, Brazil, and was funded by the *Companhia Baiana de Pesquisa Mineral*, Brazil, and in part by the *Coordenação de Aperfeiçoamento de Pessoal de Nível Superior* (CAPES), Brazil, Finance Code 001. We also thank Jailson Júnior Alves Santos for supporting the discussion of the mineral chemistry data.

ARTICLE INFORMATION

Manuscript ID: 20190041. Received on: 12/07/2018. Approved on: 04/06/2020.
R.S. performed geological mapping and collected, processed and interpreted the data, prepared the manuscript, including all figures and tables, and made the corrections suggested by reviewers; J.B. provided supervision and contributed in the field trips and improved the regional and petrological studies; A.M. provided contributions in the field trips and petrographic analyses; F.J. contributed in the geological mapping and collect of samples.
Competing interests: The authors declare no competing interests.

REFERENCES

Anhaeusser C.R. 2014. Archaean greenstone belts and associated granitic rocks - A review. *Journal of African Earth Sciences*, **100**:684-732. https://doi.org/10.1016/j.jafrearsci.2014.07.019

Anhaeusser C.R., Mason R., Viljoen M.J., Viljoen R.P. 1969. A Reappraisal of Some Aspects of Precambrian Shield Geology. *Geological Society of America Bulletin*, **80**(11):2175-2200. https://doi.org/10.1130/0016-7606(1969)80[2175:AROSAO]2.0.CO;2

Arndt N.T. 1994. Archean Komatiites. *Developments in Pre Cambrian Geology*, **11**:11-44. https://doi.org/10.1016/S0166-2635(08)70219-6

Barbosa J.S.F. 1997. Síntese do Conhecimento sobre a Evolução Geotectônica das Rochas Metamórficas Arqueanas e Paleoproterozóicas do Embasamento do Cráton do São Francisco na Bahia. *Revista Brasileira de Geociências*, **27**(3):241-256. https://doi.org/10.25249/0375-7536.1997241256

Barbosa J.S.F., Cruz S.C.P., Souza J.S. 2012a. Terrenos metamórficos do embasamento. In: Barbosa J.S.F. (Ed.). *Geologia da Bahia:* Pesquisa e Atualização. Salvador: Companhia Baiana de Pesquisa Mineral, p. 101-201. Available at: <http://www.cbpm.ba.gov.br/modules/conteudo/conteudo.php?conteudo=24>. Accessed on: Jan. 2017.

Barbosa J.S.F., Pinto M.S., Cruz S.C.P., Souza J.S. 2012b. Granitoides. In: Barbosa J.S.F. (Ed.). *Geologia da Bahia:* Pesquisa e Atualização. Salvador: Companhia Baiana de Pesquisa Mineral, p. 327-396. Available at: <http://www.cbpm.ba.gov.br/modules/conteudo/conteudo.php?conteudo=24>. Accessed on: Jan. 2017.

Barbosa J.S.F., Sabaté P. 2002. Geological features and the Paleoproterozoic collision of four Archean crustal segments of the São Francisco Craton, Bahia, Brazil. A synthesis. Rio de Janeiro, *Anais da Academia Brasileira de Ciências*, **74**(2):343-359. http://dx.doi.org/10.1590/S0001-37652002000200009

Barbosa J.S.F., Sabaté P. 2003. Colagem paleoproterozoica de placas arqueanas do Cráton do São Francisco na Bahia. *Revista Brasileira de Geociências*, **33**(1 Supl.):7-14. http://dx.doi.org/10.25249/0375-7536.200333S10714

Barbosa J.S.F., Sabaté P. 2004. Archean and Paleoproterozoic crust of the São Francisco Craton, Bahia, Brazil: geodynamic features. *Precambrian Research*, **133**(1-2):1-27. https://doi.org/10.1016/j.precamres.2004.03.001

Barbuena D., Oliveira E.P., Zincone S.A. 2016. Estudos de proveniência dos quartzitos do Greenstone Belt Mundo Novo (BA) e implicações tectono-estratigráficas. In: Congresso Brasileiro de Geologia, 48., 2016, Porto Alegre. *Anais…* , p. 818. Available at: <http://cbg2017anais.siteoficial.ws/anais48cbgcompleto.pdf>. Accessed on: Aug. 2018.

Bickle M.J., Nisbet E.G., Martin A. 1994. Archean greenstone belts are not oceanic crust. *The Journal of Geology*, **102**(2):121-137. https://doi.org/10.1086/629658

Boynton W.V. 1984. Geochemistry of the rare earth elements: meteorite studies. In: Henderson P. (Ed.). *Rare Earth Element Geochemistry*. Amsterdam: Elsevier, p. 63-114. https://doi.org/10.1016/B978-0-444-42148-7.50008-3

Chavagnac V. 2004. A geochemical and Nd isotopic study of Barberton komatiites (South Africa): implication for the Archean mantle. *Lithos*, **75**(3-4):253-281. https://doi.org/10.1016/j.lithos.2004.03.001

Condie K.C., Kronër A. 2013. The building blocks of continental crust: Evidence for a major change in the tectonic setting of continental growth at the end of the Archean. *Gondwana Research*, **23**(2):394-402. https://doi.org/10.1016/j.gr.2011.09.011

Couto P.A., Sampaio A.R., Gil C.A.A., Loureiro H.C., Arcanjo J.B., Fernandes Filho J., Guimarães J.T., Campelo R., Mascarenhas J.F., Bruni D.C., Toledo L.A.A. 1978. *Projeto Serra de Jacobina:* Geologia e Prospecção Geoquímica. Relatório Final. Salvador: Departamento Nacional de Produção Mineral - DNPM/Companhia de Pesquisa de Recursos Minerais - CPRM, 415 p. Available at: <http://rigeo.cprm.gov.br/jspui/handle/doc/9602>. Accessed on: Apr. 2018.

De Wit M.J., Hart R.A., Hart R.J. 1987. The Jamestown ophiolite complex, Barberton Mountain Belt: a section through 3.5 Ga oceanic crust. *Journal of African Earth Sciences*, **6**(5):681-730. https://doi.org/10.1016/0899-5362(87)90007-8

Elhlou S., Belousova E., Griffin W.L., Pearson N.J., O'Reilly S.Y. 2006. Trace element and isotopic composition of GJ red zircon standard by laser ablation. *Geochimica et Cosmochimica Acta*, **70**(18 Suppl.):A158. https://doi.org/10.1016/j.gca.2006.06.1383

Fettes D.J., Desmons J., Árkai P., Brodie K., Bryhni I. 2007. *Metamorphic rocks*: a classification and glossary terms. Cambridge: Cambridge University Press. 244 p. Available at: <https://lib.ugent.be/catalog/rug01:001234988>. Accessed on: Jan. 2018.

Furnes H., de Wit M., Robins B. 2013. A review of new interpretations of the tectonostratigraphy, geochemistry and evolution of the Onverwacht Suite, Barberton Greenstone Belt, South Africa. *Gondwana Research*, **23**(2):403-428. https://doi.org/10.1016/j.gr.2012.05.007

Grachev A.F., Pechersky D.M., Tsel'movich V.A. 2011. Titanomagnetites and ilmenites from the Early Cenozoic Basalts and Limburgites of the Northern Tien Shan. *Physics of the Solid Earth*, **47**:475-487. https://doi.org/10.1134/S106935131105003X

Herzberg C. 1995. Generation of plume magmas through time: an experimental perspective. *Chemical Geology*, **126**(1):1-16. https://doi.org/10.1016/0009-2541(95)00099-4

Hofmann A.W. 1988. Chemical differentiation of the Earth: the relationship between mantle, continental crust, and oceanic crust. *Earth and Planetary Science Letters*, **90**(3):297-314. https://doi.org/10.1016/0012-821X(88)90132-X

Irvine T.N., Baragar W.R.A. 1971. A guide to the Chemical Classification of the Common Volcanic Rocks. *Canadian Journal of Earth Sciences*, **8**(5):523-548. https://doi.org/10.1139/e71-055

Jahn B.M., Gruau G., Glikson A.Y. 1982. Komatiites of the Onverwacht Group, S. Africa: REE Geochemistry, Sm/Nd Age and Mantle Evolution. *Contributions to Mineralogy and Petrology*, **80**:25-40. https://link.springer.com/article/10.1007/BF00376732

Janousek V., Farrow C.M., Erban V. 2006. Interpretation of whole-rock geochemical data in igneous geochemistry: introducing Geochemical Data Toolkit (GCDkit). *Journal of Petrology*, **47**(6):1255-1259. https://doi.org/10.1093/petrology/egl013

Jensen L.S. 1976. *A new cation plot for classifying subalkalic volcanic rocks*. Ontario: Ontario Division of Mines, Miscellaneous Paper 66, 22 p. Available at: <http://www.geologyontario.mndmf.gov.on.ca/mndmfiles/pub/data/imaging/MP066/MP066.pdf>. Accessed on: Jan. 2018.

Jochum K.P., Arndt N.T., Hofmann A.W. 1991. Nb-Th-La in komatiites and basalts; constraints on komatiite petrogenesis and mantle evolution. *Earth Planetary Science Letters*, **107**(2):272-289. https://doi.org/10.1016/0012-821X(91)90076-T

Kerrich R., Xie Q. 2002. Compositional recycling structure of an Archean super-plume: Nb-Th-U-LREE systematics of Archean komatiites and basalts revisited. *Contributions to Mineralogy and Petrology*, **142**:476-484. https://doi.org/10.1007/s004100100301

Kretz R. 1983. Symbols for rock-forming minerals. *American Mineralogist*, **68**(1):277-279. Available at: <https://www.researchgate.net/publication/216831138_Symbols_for_rock-forming_minerals>. Accessed on: Feb. 2018.

Leake B.E., Woolley A.R., Arps C.E.S., Birch W.D., Gilbert M.C., Grice J.D., Hawthorne F.C., Kato A., Kisch H.J., Krivovichev V.G., Linthout K., Laird J., Mandarino J.A., Maresch W.V., Nickel E.H., Rock N.M.S., Schumacher J.C., Smith D.C., Stephenson N.C.N., Ungaretti L., Whittaker E.J.W., Youzhi G. 1997. Nomenclature of Amphiboles: Report of the Subcommittee on Amphiboles of the International Mineralogical Association Commission on New Minerals and Mineral Names. *The Canadian Mineralogist*, **35**(1):219-246.

Leal L.R.B. 1998. *Geocronologia U/Pb (SHRIMP), 207Pb/206Pb, Rb/Sr, Sm/Nd e K/Ar dos Terrenos Granito-Greenstone do Bloco do Gavião: Implicações para a Evolução Arqueana e Paleoproterozoica do Cráton do São Francisco, Brasil*. PhD Thesis, Universidade de São Paulo, São Paulo, 178 p. Available at <http://www.teses.usp.br/teses/disponiveis/44/44134/tde-08012016-145912/pt-br.php>. Accessed on: Sept., 2018. https://doi.org/10.11606/T.44.2016.tde-08012016-145912

Leal L.R.B., Cunha J.C., Cordani U.G., Teixeira W., Nutman A.P., Leal A.B.M., Macambira M.J.B. 2003. Shrimp U-Pb, $^{207}Pb/^{206}Pb$ zircon dating, and Nd isotopic signature of the Umburanas greenstone belt, northern São Francisco craton, Brazil. *Journal of South American Earth Sciences*, **15**(7):775-785. https://doi.org/10.1016/S0895-9811(02)00129-3

Leite C.M.M. 2002. *A Evolução Geodinâmica da Orogênese Paleoproterozóica nas Regiões de Capim Grosso, Jacobina e Pintadas - Mundo Novo (Bahia-Brasil): Metamorfismo, Anatexia Crustal e Tectônica*. PhD Thesis, Universidade Federal da Bahia, Salvador, 408 p.

Leite C.M.M., Barbosa J.S.F., Nicollet C., Sabaté P. 2007. Evolução metamórfica/metassomática paleoproterozóica do Complexo Saúde, da Bacia Jacobina e de leucogranitos peraluminosos na parte norte do Cráton do São Francisco. *Revista Brasileira de Geociências*, **37**(4):777-797. https://doi.org/10.25249/0375-7536.2007374777797

Loureiro H.S.C. 1991. *Programa Levantamentos Geológicos Básicos do Brasil. Mundo Novo. Folha SC24-Y-D-IV. Estado da Bahia*. Salvador: Departamento Nacional de Produção Mineral - DNPM/Companhia de Pesquisa de Recursos Minerais - CPRM, 177 p. Available at: <http://rigeo.cprm.gov.br/jspui/handle/doc/8498>. Accessed on: Oct. 2017.

Ludwig K.R. 2001. *SQUID 1.03:* A User's Manual. Berkeley, Berkeley Geochronology Center, Special Publication, **2**, 17 p.

Ludwig K.R. 2003. *User's manual for ISOPLOT 3.00*. A geochronological toolkit for Microsoft Excel. Berkeley, Berkeley Geochronology Center, Special Publication, **4**, 70 p.

Lynch L. 1996. Provisional elemental values for four new geochemical soil and till reference materials, TILL-1, TILL-2, TILL-3 and TILL-4. *Geostandards and Geoanalytical Research*, **20**(2):277-287. https://doi.org/10.1111/j.1751-908X.1996.tb00189.x

Magee C.W., Palin J.M., Taylor W.R. 2001. Laser ICP-MS U/Pb analyses of detrital zircons from Proterozoic sediments in Bahia state, Brazil; implications for the evolution of the São Francisco craton prior to 3.3 Ga. In: V.M. Goldschmidt Conference, 11., 2001, Hot Springs. *Abstracts…*, p. 3501. Available at: <https://www.lpi.usra.edu/meetings/gold2001/pdf/3501.pdf>. Accessed on: Nov. 2017.

Mascarenhas J.F., Guimarães J.T., Moraes L.C., Queiroz C.J.A., Marinho M.M., Neves J.P. 1975. *Projeto Bahia:* Geologia da Folha de Senhor do Bonfim. Relatório Final. Salvador: Departamento Nacional de Produção Mineral - DNPM/Companhia de Pesquisa de Recursos Minerais.

Mascarenhas J.F., Ledru P., Souza S.L., Conceição Filho V.M., Melo L.F.A., Lorenzo C.L., Milesi J.P. 1998. *Geologia e recursos minerais do Grupo Jacobina e da parte sul do Greenstone Belt de Mundo Novo*. (Série Arquivos Abertos, **13**.) 58 p. Available at: <http://www.cbpm.ba.gov.br/modules/conteudo/conteudo.php?conteudo=23>. Accessed on: Mar. 2016.

Mascarenhas J.F., Silva E.F.A. 1994. *Greenstone Belt de Mundo Novo: caracterização e implicações metalogenéticas no Cráton do São Francisco*. Série Arquivos Abertos, **5**, 32 p. Available at: <http://www.cbpm.ba.gov.br/modules/conteudo/conteudo.php?conteudo=23>. Accessed on: Mar. 2016.

Middlemost E.A.K. 1994. Naming materials in the magma/igneous rock system. *Earth Science Reviews*, **37**(3-4):215-224. https://doi.org/10.1016/0012-8252(94)90029-9

Morimoto N. 1988. Nomenclature of pyroxenes. *Mineralogy and Petrology*, **39**:55-76. Available at: <https://link.springer.com/article/10.1007/BF01226262>. Accessed on: Apr. 2019. https://doi.org/10.1007/BF01226262

Mougeot R. 1996. *Étude de la limite Archéen-Protérozoïque et des minéralisations Au ± U associées. Exemples de la région de Jacobina (Etat de Bahia, Brésil) et de Carajas (Etat de Para, Brésil)*. PhD Thesis, Université de Montpellier II, Montpellier, 306 p. Available at <http://www.theses.fr/1996MON20131>. Accessed on: Sept., 2018.

Oliveira E.P., McNaughton N.J., Armstrong R. 2010. Mesoarchaean to Paleoproterozoic growth of the northern segment of the Itabuna-Salvador-Curaçá orogeny, São Francisco Cráton, Brazil. In: Kusky T.M., Zhai M.G., Xiao W. (Eds.). *The evolving continents:* understanding processes of continental growth. Geological Society of London Special Publication, **338**(1):263-286. https://doi.org/10.1144/SP338.13

Oliveira E.P., Mello E.F., McNaughton N. 2002a. Reconnaissance U-Pb geochronology of Precambrian quartzites from the Caldeirão belt and their basement, NE São Francisco Craton, Bahia, Brazil: implications for the early evolution of the Paleoproterozoic Itabuna-Salvador-Curaçá orogeny. *Journal of South American Earth Sciences*, **15**(3):349-362. https://doi.org/10.1016/S0895-9811(02)00039-1

Oliveira E.P., Mello E.F., McNaughton N.J., Choudhuri A. 2002b. SHRIMP U-Pb age of the basement to the Rio Itapicuru Greenstone Belt, NE São Francisco craton. In: Congresso Brasileiro de Geologia, 41., 2002, João Pessoa. *Anais…*, p. 522.

Parman S.W., Dann J.C., Grove T.L., De Wit M.J. 1997. Emplacement conditions of komatiite magmas from the 3.49 Ga Komati Formation, Barberton greenstone Belt, South Africa. *Earth and Planetary Science Letters*, **150**(3-4):303-323. https://doi.org/10.1016/S0012-821X(97)00104-0

Parman S.W., Grove T.L., Dann J.C. 2001. The production of Barberton komatiites in an Archean subduction zone. *Geophysical Research Letters*, **28**(13):2513-2516. https://doi.org/10.1029/2000GL012713

Pearce J.A. 2005. Mantle preconditioning by melt extraction during flow: theory and petrogenetic implications. *Journal of Petrology*, **46**(5):973-997. https://doi.org/10.1093/petrology/egi007

Pearce J.A. 2008. Geochemical fingerprinting of oceanic basalts with applications to ophiolite classification and the search for Archean oceanic crust. *Lithos*, **100**(1-4):14-48. https://doi.org/10.1016/j.lithos.2007.06.016

Pearce J.A. 2014. Geochemical fingerprinting of the Earth's Oldest Rocks. *Geology*, **42**(2):175-176. https://doi.org/10.1130/focus022014.1

Pearce J.A., Harris N.B.W., Tindle A.G. 1984. Trace element discrimination diagrams for the tectonic interpretation of granitic rocks. *Journal of Petrology*, **25**(4):956-983. https://doi.org/10.1093/petrology/25.4.956

Pearce J.A., Parkinson I.J. 1993. Trace element models for mantle melting: application to volcanic arc petrogenesis. In: Prichard H.M., Alabaster T., Harris N.B.W., Neary C.R. (Eds.). *Magmatic Processes and Plate Tectonics*. Geological Society of London Special Publication, **76**:373-403. https://doi.org/10.1144/GSL.SP.1993.076.01.19

Pearce J.A., Stern R.J., Bloomer S.H., Fryer P. 2005. Geochemical mapping of the Mariana Arc-Basin System: implications for the nature and distribution of subduction components. *Geochemistry, Geophysics, Geosystems*, **6**(7):1-27. https://doi.org/10.1029/2004GC000895

Peucat J.J., Mascarenhas J.F., Barbosa J.S.F., Souza S.L., Marinho M.M., Fanning C.M., Leite C.M.M. 2002. 3,3 Ga SHRIMP U-Pb zircon age of a felsic metavolcanic rock from the Mundo Novo Greenstone Belt in the São Francisco Craton, Bahia (NE Brazil). *Journal of South American Earth Sciences*, **15**(3):363-373. https://doi.org/10.1016/S0895-9811(02)00044-5

Polat A., Hoffmann A.W. 2003. Alteration and geochemical patterns in the 3.7-3.8 Ga Isua greenstone belt, West Greenland. *Precambrian Research*, **126**(3-4):197-218. https://doi.org/10.1016/S0301-9268(03)00095-0

Polat A., Hoffmann A.W., Rosing M.T. 2002. Boninite-like volcanic rocks in the 3.7-3.8 Ga Isua greenstone belt, West Greenland: geochemical evidence for intra-oceanic subduction zone processes in the early Earth. *Chemical Geology*, **184**(3-4):231-254. https://doi.org/10.1016/S0009-2541(01)00363-1

Polat A., Kerrich R. 2001. Magnesian andesites, Nb-enriched basalt-andesites, and adakites from late-Archean 2.7 Ga Wawa greenstone belts, Superior Province, Canada: implications for late Archean subduction zone petrogenetic processes. *Contributions to Mineralogy and Petrology*, **141**:36-52. https://doi.org/10.1007/s004100000223

Ramsay J.G., Huber M.I. 1987. *The techniques of Modern Structural Geology*. Folds and Fractures. London, Pergamon Press, **2**, 703 p.

Reis C., Menezes R.C.L., Miranda D.A., Santos F.P., Loureiro H.C., Neves J.P., Viera R. 2017. *Mapa geológico-geofísico: Projeto ARIM Serra de Jacobina*. Salvador: Companhia de Pesquisa de Recursos Minerais - CPRM. Available at: <http://rigeo.cprm.gov.br/jspui/handle/doc/18679>. Accessed on: Jun. 2018.

Reis C., Oliveira R.C.L., Miranda D.A., Santos F.P., Guimarães J.T., Teles G. 2018. Estratigrafia do grupo Jacobina. In: Congresso Brasileiro de Geologia, 49., 2018, Rio de Janeiro, *Anais*, p. 1232. Available at: <http://cbg2018anais.siteoficial.ws/resumos/7641.pdf>. Accessed on: Sep. 2018.

Rios C.V. 2017. *Geologia isotópica das formações ferríferas bandadas do Cráton São Francisco na transição Arqueano Paleoproterozoico*. PhD Thesis, Instituto de Geociências, Universidade de Brasília, Brasília, 243 p.

Rios D.C., Davis D.W., Conceição H., Davis W.J., Rosa M.L.S., Dickin A.P. 2009. Geologic evolution of the Serrinha nucleus granite-greenstone terrane (NE Bahia, Brazil) constrained by U-Pb single zircon geochronology. *Precambrian Research*, **170**(3-4):175-201. https://doi.org/10.1016/j.precamres.2008.10.001

Rollinson H.R. 1993. *Using Geochemical Data:* Evaluation, Presentation, Interpretation. England, Longman Scientific and Technical, 352 p.

Sabaté P., Marinho M.M., Vidal P., Caen-Vachette M. 1990. The 2-Ga peraluminous magmatism of the Jacobina–Contendas Mirante belts (Bahia, Brazil): geologic and isotopic constraints on the sources. *Chemical Geology*, **83**(3-4):325-338. https://doi.org/10.1016/0009-2541(90)90288-I

Schmid R., Fettes D., Harte B., Davis E., Desmons J. 2007. *How to name a metamorphic rock*. Recommendations by the IUGS Subcommission on the Systematics of Metamorphic Rocks. IUGS Commission on the Systematics in Petrology. Available at: <www.bgs.ac.uk/scmr/home.html>. Accessed on: Sept. 2018.

Siivola J., Schmid R. 2007. *A systematic nomenclature for metamorphic rocks*. 12. List of mineral abbreviations. Recommendations by the IUGS Subcommission on the Systematics of Metamorphic Rocks. IUGS Commission on the Systematics in Petrology. Available at: <https://www.bgs.ac.uk/downloads/start.cfm?id=3197>. Accessed on: Nov. 2017.

Silva L.C., Armstrong R., Delgado I.M., Pimentel M., Arcanjo J.B., Melo R.C., Teixeira L.R., Jost H., Cardoso Filho J.M., Pereira L.H.M. 2002. Reavaliação da evolução geológica em terrenos Pré-Cambrianos brasileiros com base em novos dados U-Pb SHRIMP, Parte I: Limite centro-oriental do Cráton São Francisco na Bahia. *Revista Brasileira de Geociências*, **32**(4):501-512. https://doi.org/10.25249/0375-7536.2002324501512

Silva L.C., McNaughton N.J., Melo R.C., Fletcher I.R. 1997. U-Pb SHRIMP ages in the Itabuna-Caraíba TTG high-grade complex: the first window beyond the Paleoproterozoic overprinting of the eastern Jequié Craton, NE Brazil. In: Isgam International Symposium on Granites and Associated Mineralization, 1., 1997, Salvador. *Abstracts…* , p. 282-283. Available at: <https://www.researchgate.net/publication/284106273>. Accessed on: Oct. 2017.

Sousa D.F.M., Oliveira E.P., Amaral W.S. 2018. Geologia e geocronologia U-Pb em zircão de ortognaisses e K-granitoides relacionados ao Bloco Gavião (Complexo Mairi) e Cinturão Salvador-Curaçá – Região da Mina Caraíba – Bahia. In: Congresso Brasileiro de Geologia, 49., 2018, Rio de Janeiro. *Anais*..., p. 980. Available at: <http://cbg2018anais.siteoficial.ws/resumos/8534.pdf>. Accessed on: Aug. 2018.

Souza S.L., Garrido I.A.A., Oliveira N.S., Fróes R.J. 2002. *Projeto Greenstone Belt de Mundo Novo:* estudos geológicos regionais. Salvador: Companhia Baiana de Pesquisa Mineral - CBPM, **1**, 62 p.

Spreafico R.R. 2017. *Projeto Mundo Novo:* texto e mapas. Salvador: Companhia Baiana de Pesquisa Mineral - CBPM, 84 p.

Spreafico R.R., Barbosa J.S.F., Barbosa N.S., Moraes A.M.V., Souza Júnior F.D. A idade Neoarqueana (2,59 Ga, U-Pb) do *greenstone belt* Mundo Novo, Bahia, Brasil. In: Congresso Brasileiro de Geologia, 49., 2018, Rio de Janeiro. *Anais*..., p. 1930. Available at: <http://cbg2018anais.siteoficial.ws/resumos/7518.pdf>. Accessed on: Sep. 2018.

Storey M., Saunders A.D., Tarney J., Leat P.T., Thirlwall M.F., Thompson R.N., Menzies M.A., Marriner G.F. 1988. Geochemical evidence for plume-mantle interactions beneath Kerguelen and Heard Islands, Indian Ocean. *Nature*, **336**:371-374. https://doi.org/10.1038/336371a0

Teles G.S. 2013. *Proveniência e idades de deposição dos sedimentos auríferos da Bacia de Jacobina: Implicações sobre a evolução da bacia durante o Paleo-Arqueano e a gênese da mineralização*. MS Dissertation, Instituto de Geociências, Universidade de Brasília, Brasília, 122 p. Available at: <http://repositorio.unb.br/handle/10482/14972>. Accessed on: July 2018.

Teles G.S., Chemale Jr. F., Oliveira C.G. 2015. Paleoarchean record of the detrital pyrite-bearing, Jacobina Au-U deposits, Bahia, Brazil. *Precambrian Research*, **256**:289-313. https://doi.org/10.1016/j.precamres.2014.11.004

Thompson M. 1988. Variation of precision with concentration in an analytical system. *Analyst*, **113**(10):1579-1587. https://doi.org/10.1039/AN9881301579

Whitney D.L., Evans B.W. 2010. Abbreviations for names of rock-forming minerals. *American Mineralogist*, **95**(1):185-187. https://doi.org/10.2138/am.2010.3371

Wilson N. 1987. *Combined Sm-Nd, Pb-Pb and Rb-Sr geochronology and isotope geochemistry in polymetamorphic Precambrian terrains: examples from Bahia, Brazil and Channel Island*. MS Dissertation, U.K. Master, Oxford University, England, 150 p.

Xie Q., Kerrich R. 1994. Silicate–perovskite and majorite signature komatiites from the Archean Abitibi greenstone belt; implications for early mantle differentiation and stratification. *Journal of Geophysical Research*, **99**(B8):15799-15812. https://doi.org/10.1029/94JB00544

Zincone S.A., Barbuena D., Oliveira E.P., Baldim M.R. 2017. Detrital zircon U-Pb ages as evidence for deposition of the Saúde Complex in a Paleoproterozoic foreland basin, northern São Francisco Craton, Brazil. *Journal of South American Earth Sciences*, **79**:537-548. https://doi.org/10.1016/j.jsames.2017.09.009

Zincone S.A., Oliveira E.P., Laurent O., Zhang H., Zhai M. 2016. 3.3 Ga High-Silica Intraplate Volcanic-Plutonic System of the Gavião Block, São Francisco Craton, Brazil: Implications of an intracontinental rift following the creation of insulating continental crust. *Lithos*, **266-267**:414-434. https://doi.org/10.1016/j.lithos.2016.10.011

Zucchetti M., Lobato L.M., Baars F.J. 2000a. Genetically diverse basalt geochemical signatures developed in the Rio das Velhas greenstone belt, Quadrilátero Ferrífero, Minas Gerais, Brazil. *Revista Brasileira de Geociências*, **30**(3):397-402.

Zucchetti M., Lobato L.M., Baltazar O.F. 2000b. Volcanic and volcaniclastic features in Archean rocks and their tectonic environments, Rio das Velhas greenstone belt, Quadrilátero Ferrífero, MG - Brazil. *Revista Brasileira de Geociências*, **30**(3):388-392.